Applying Adaptive Optics and Quantum Dots to Stochastic Optical Reconstruction Microscopy

by

Andrew Traylor Herrington

(Under the Direction of Peter A. Kner)

Abstract

Stochastic optical reconstruction microscopy (STORM) constructs groundbreaking images of biological structures in a completely native environment. This allows previously diffraction limited systems to image structures to 20 nm of resolution. Theoretically the resolution gain is only limited by the number of photons a fluorophore emits. The dyes and proteins typically used as fluorophores photobleach rapidly with small average photon counts. Quantum dots, however, have a much higher brightness than these conventional markers but lack a controllable blinking mechanism. A new technique that causes quantum dots to blink, called "blueing", will be examined for use with STORM. In a unique approach to capture 3D images, a deformable mirror is used to provide a controlled amount of astigmatism to the image plane.

Index words: Superresolution, Fluorescence, Microscopy, Photoactivated Localization Microscopy (PALM), Stochastic Optical Reconstruction Microscopy (STORM), Adaptive Optics

Applying Adaptive Optics and Quantum Dots to Stochastic Optical Reconstruction Microscopy

by

Andrew Traylor Herrington

B.S., Georgia Institute of Technology, 2008

A Thesis Submitted to the Graduate Faculty
of The University of Georgia in Partial Fulfillment
of the
Requirements for the Degree

Master of Science

Athens, Georgia

2012

©2012

Andrew Traylor Herrington

All Rights Reserved

APPLYING ADAPTIVE OPTICS AND QUANTUM DOTS TO STOCHASTIC OPTICAL RECONSTRUCTION MICROSCOPY

by

ANDREW TRAYLOR HERRINGTON

Approved:

Major Professor: Peter A. Kner

Committee: Mark A. Haidekker
William S. Kisaalita

Electronic Version Approved:

Dr. Maureen Grasso
Dean of the Graduate School
The University of Georgia
December 2012

Acknowledgments

I would like to take this page to express my deepest gratitude and respect for all parties involved in the undertaking of this thesis. It took collaboration both inside and out of the lab. I am especially grateful to my major professor, Dr. Peter Kner, for his ongoing and tireless effort to support me throughout this work. Through his guidance I have bettered myself as a researcher and student.

I'd also like to thank my committee members, Dr. William Kisaalita and Dr. Mark Haidekker, for their time and good nature throughout my two years at the University of Georgia.

The pictures of *Toxoplasma gondii* would not be possible without the help of Maria Francia and Dr. Boris Striepen's lab here at UGA. All other samples were contributed by the QSTORM team: Dr. Jessica Winter's group at Ohio State University, Dr. Ge Yang's group at Carnegie Mellon and Dr. Beth Brainerd's group at Brown University.

Finally a thank you to my lab mates who were always there to provide humor and perspective. Most importantly I appreciate my friends and family who have supported me throughout my life regardless of the challenges I face.

Contents

List of Figures

List of Tables

Nomenclature

Δx	Error in localization, see equation (2.1)
ε_{abs}	Molar extinction coefficient, see equation (3.1)
λ	Wavelength, see equation (1.1)
σ	Absorption cross-section, see equation (3.2)
τ_0	Excitation rate to excited state, see equation (3.2)
τ_1	Lifetime of the excited state, see equation (3.2)
τ_2	Intersystem crossing rate, see equation (3.3)
τ_3	Lifetime of the triplet state, see equation (3.2)
φ	Fluorescence quantum yield, see equation (3.1)
A	Actuator voltage array, see equation (5.1)
a	Variance of the top-hat distribution, see equation (2.2)
ADC	CCD value for a given pixel, see equation (6.1)
b	Standard deviation of the background noise, see equation (2.3)
G	EM gain level, see equation (6.1)
H	Influence function array, see equation (5.1)
N	Number of photons detected, see equation (2.1)
R	Resolution, see equation (1.1)
S	CCD sensitivity, see equation (6.1)
s	Width of the point spread function, see equation (2.1)
W	Wavefront, see equation (5.1)
AO	Adaptive Optics
BME	β-Mercaptoethanol
BPFPALM	Biplane Fluorescence Photoactivation Localization Microscopy
BSA	Bovine Serum Albumin
CCD	Charged Couple Device
DH-PSF	Double-Helix Point Spread Function
DM	Deformable Mirror

dSTORM	Direct Stochastic Optical Reconstruction Microscopy
EM	Electron Multiplying
FIONA	Fluorescence Imaging with One-Nanometer Accuracy
FPALM	Fluorescence Photoactivation Localization Microscopy
FWHM	Full Width at Half Maximum
GFP	Green Fluorescence Protein
GS	Gerchberg-Saxton
GSDM	Ground State Depletion Microscopy
ICA	Independent Component Analysis
IML-SPIM	Individual Molecule Localization-Selective Plane Illumination Microscopy
iPALM	Interferometric Photoactivated Localization Microscopy
KL	Kullback-Leibler
LM	Light Microscopy
MEA	Monoethanolamine
MRI	Magnetic Resonance Imaging
NGS	Normal Goat Serum
OPT	Optical Projection Tomography
PA-GFP	Photoactivated-Green Fluorescence Protein
PALM	Photoactivated Localization Microscopy
PBS	Phosphate Buffered Saline
PBT	Phosphate Buffered Saline Triton-X100
PL	Photoluminescence
PSF	Point Spread Function
QD	Quantum Dot
ROXS	Reducing and Oxidizing System
SIM	Structured Illumination Microscopy
SLM	Spatial Light Modulator
SNR	Signal-to-Noise Ratio
SOFI	Superresolution Optical Fluctuation Imaging
STED	Stimulated Emission Depletion
STORM	Stochastic Optical Reconstruction Microscopy
TEM	Transmission Electron Microscopy
TIRF	Total Internal Reflection Microscopy

Chapter 1

Introduction

1.1 Light Microscopy

The light microscope invented in the mid-17th century, images biological samples using visible light and a system of lenses. Light illuminates a lens beneath the stage, called a condenser, travels through the sample, through an objective lens and then to a camera or eye via a second magnifying lens, the ocular. The light can be scattered, transmitted or emitted by the sample. Different forms of light microscopy (LM) achieve contrast by measuring the different interactions of the incident light with the sample.

Fluorescence microscopy, seen in Figure 1.1, is perhaps the most important form of LM for biological applications. Using a light source (e.g. a laser or LED), certain wavelengths push the fluorophores into an excited state through photon absorption. As these fluorophores drop back down to the ground state, they emit a red-shifted photon of light. The loss of energy, due to vibration, between the absorbed and emitted photons is known as the Stokes Shift (Figure 1.2). There exist many molecules in nature that have an inherent fluorescence (e.g. NAD(P)H). However, researchers most often introduce exogenic fluorescent molecules, either dyes or proteins, called fluorophores, to tag the molecules of interest [1].

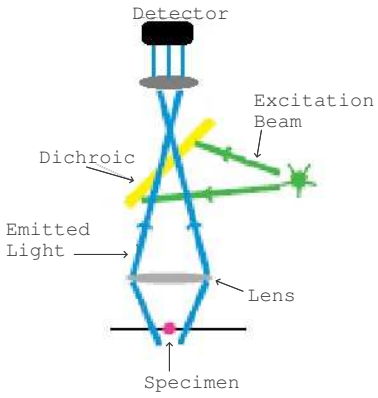

Figure 1.1: In this general schematic of a widefield fluorescence microscope, an excitation beam is reflected off of a dichroic lens toward the sample, exciting the fluorophores. In a fluorescence microscopy, fluorescent molecules are excited with light at a particular wavelength. Photons are emitted by the molecules back toward the dichroic, but are allowed to pass through because they are at a longer wavelength. The emitted light is then imaged onto the detector, which is usually a CCD camera.

The fluorophore's emitted photons travel to a charged coupled device (CCD) camera. Widefield systems capture the entire plane of the specimen at once instead of having to scan it. The speed of acquisition and ability to use filter wheels allows for fast switching between various excitation wavelengths. This opposes confocal scanning laser microscopy which eliminates much of the background light by slowly scanning over a specimen, and only collecting light that passes through a pinhole (examined in more detail in Section 1.3). However, the scanning process is too slow for fast biological events.

Light microscopy has the distinct advantage over other forms of microscopy for being ideal at imaging live cells. Electron microscopy can reach 0.05 nm resolution, but requires the sample to be stained with a heavy metal (e.g. lead, uranium or gold) and imaged in vacuum. Scanning probe microscopy can only image the cell surface and requires contact for accurate data which would

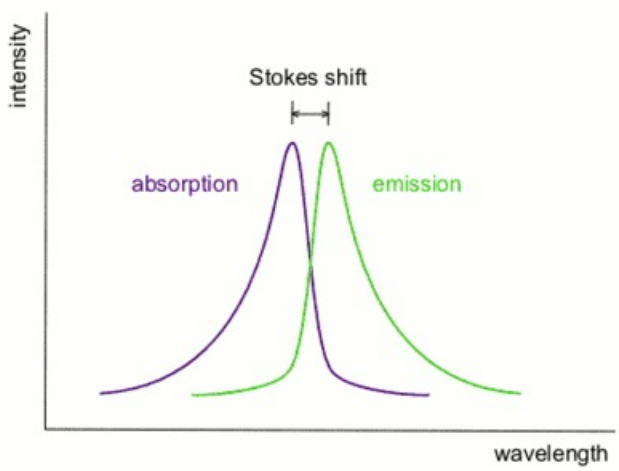

Figure 1.2: The Stokes shift is the difference in wavelength after a fluorophore absorbs a photon of higher wavelength, entering into an excited state, and then relaxes by emitting a photon of shorter wavelength.

potentially damage biological samples. Non-contact forms exist, but the inability to image past the surface makes it impossible to view any metabolic pathways or live cell environments.

Unfortunately, fluorescence microscopy has its limitations. Conventional light microscopy is unable to view molecules at the nanometer level of resolution. The wave nature of light imposes a fundamental restriction on spatial resolution of approximately 200 nm [2]. This proves problematic, as the nanometer scale structure of cells and proteins is linked to their biological functions. While fluorescence microscopy is diffraction limited, it can not provide more detailed information on live cells.

1.2 Diffraction Limit

The spatial resolution LM offers is limited by diffraction within the optical system. George Biddell Airy states that a uniformly lit circular aperture has a diffraction pattern with a bright spot in the

middle and concentric rings around it. As shown in Figure 1.3, the image of a point has a finite width due to the finite aperture of the microscope.

The image of a point source is known as the Airy disk (Figure 1.3). The Rayleigh Criterion,

$$R = \frac{0.61 * \lambda}{NA} \tag{1.1}$$

defines the resolution of an optical microscope as the minimum distance between two point sources such that their presence can be distinguished in the image (R = Resolution, λ = Wavelength and NA = Numerical Aperture) [3]. Because point sources of light appear as Airy disks, when the center of one Airy disk falls on the first minimum of the Airy pattern of another, the two are considered just resolved. Any closer and the two points will be irresolvable (Figure 1.4).

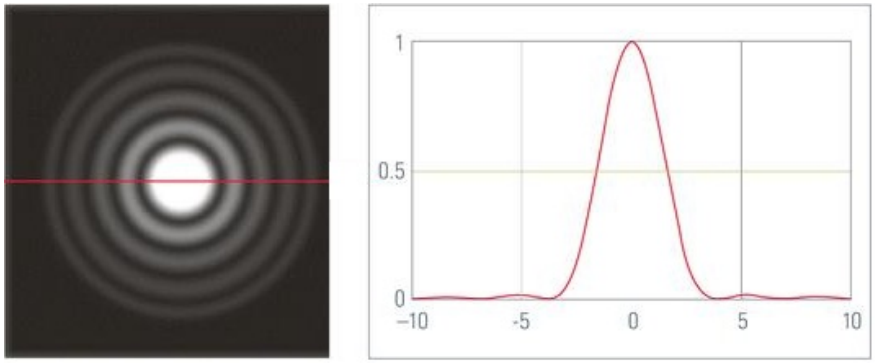

Figure 1.3: The Airy disk diffraction pattern created by a circular lens. **(Left)** The airy disc with the middle point saturated (e.g. max recordable intensity) so the surrounding rings may be seen. **(Right)** A line profile taken from the left image.

In an optical system, the wavelength of light, design of the lens, and the numerical aperture all affect the resolution. So for a numerical aperture of 1.28 and wavelength of 488 nm, this gives a resolution of 232 nm, diffraction of light being the root cause of the resolution limit.

Even with perfect lenses, alignment, and large numerical apertures the optical resolution of LM was limited to about half the wavelength of the excitation light. This limit, however, is still difficult

Figure 1.4: These images demonstrate the Rayleigh criterion. **(a)** Two point sources of light that are neighboring one another, yet have a far enough distance apart that they may be individually resolved. **(b)** The same sources but are now only just resolved by a minimum required distance to distinguish between two points. **(c)** Two points completely overlaid upon one another reaching the resolution limit [4].

to attain as it requires a homogeneous refractive index, high signal intensity and low background signals. One widely used method to increase the signal-to-noise ratio is the deconvolution of wide-field image z-stacks [5].

The point spread function (PSF) is the image made by the microscope of a point source of light, in 2D this is the Airy disc. This shape represents the PSF of the microscope system. The image made by a microscope is the convolution of the sample structure with the PSF. Using computer based post processing methods, this convolution can be undone to some extent. The final image having a less out of focus light.

In confocal laser scanning microscopy a tightly focused spot of laser light is scanned over a sample. The emitted light is focused onto a pinhole sized aperture. This only allows light originating from the nominal focus to pass removing out of focus light [6]. Both deconvolution and confocal laser scanning have been considered the gold standard in bioimaging, however there have recently been multiple approaches to resolve even smaller details.

1.3 Super-resolution Microscopy

Rayleigh's Criterion, however, uses a deterministic model and is appropriate for the case when many objects are being imaged at once [3]. This is suitable for conventional widefield imaging. When there is *a priori* knowledge, however, the Rayleigh limit can be broken. Knowing there are only two points closer than the Rayleigh Criterion allows for the localization of each individually. By instead using a stochastic framework, imaging small numbers of fluorophores and taking into account the number of detected photons, the diffraction limit can be easily broken.

Equation 1.1 is the theoretical resolution limit of a microscope. Any technique which resolves images below this limit is considered to be super-resolution microscopy. Two deterministic methods enable researchers to peer past the Rayleigh's Criterion. Structured illumination microscopy (SIM), taking advantage of Fourier optics, doubles resolution in three dimensions.

SIM [7, 8] takes images of samples with superposed (multiplied) line patterns that create moiré fringes. A sinusoidal striped illumination pattern has three Fourier components. If a sample is illuminated with such light, moiré fringes will appear which represent three shifted copies of the sample in reciprocal space. The amount of the shift corresponds to the three Fourier components of the illumination. From a sequence of images with different patterns an image is created with twice the original resolution, about 100 nm.

Stimulated emission depletion (STED) [9] can achieve resolutions of 50 nm [10]. STED acts by depleting the outside of a confocal spot, while leaving a much narrower center focal spot to excite fluorescence, seen in Figure 1.5. The focal area left active can be engineered with diffractive optical elements. This narrow excitation spot is then scanned over the sample resulting in a resolution determined by the width of the spot.

Auspiciously in 2006, a new stochastic technique discovered by multiple groups shattered the previous resolution barriers. These papers [11, 12, 13] described a new technique which can achieve lateral resolutions of 20 nm and axial resolutions of 50 nm, allowing scientists to see

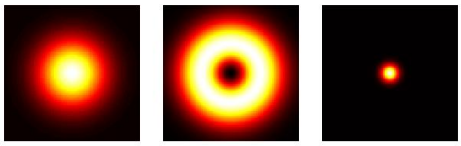

Figure 1.5: **(Left)** The excitation spot, **(Center)** the dump or de-excitation area and **(Right)** the resulting area causing fluorescence.

ground breaking new features. Each described the same fundamental process with different names: stochastic optical reconstruction microscopy (STORM), photoactivated localization microscopy (PALM) and fluorescence photoactivation localization microscopy (FPALM).

1.4 Thesis Objectives

For this thesis, we develop a STORM system starting with a conventional fluorescence microscope. Then we explore improving the performance of STORM using quantum dots and adaptive optics. Through the use of a deformable mirror we will correct aberrations found within our own system using only intensity based data (i.e. without a wavefront sensor). Furthermore, adaptive optics may be used to extend STORM into thick samples. Typically STORM is only used on thin samples.

Another objective, in a novel technique, uses the deformable mirror instead of a cylindrical lens to project controlled aberrations onto samples creating an astigmatic image. This is used in conjunction with STORM to create a 3D image by correlating bead depth to symmetry of an object.

Resolution is not only limited by the signal-to-noise ratio, the number of photons captured also influences the resolution of STORM. Nanoparticles, mounting buffers, excitation procedures and their relationship with photon counts will each be examined and compared. Quantum dots exhibit many favorable features, including higher photon counts than conventional probes. They

are unable, it seems, to blink in a controlled way that allows for densely labeled samples to be imaged. A technique called blueing is examined to circumvent this limitation.

In the next two chapters we will describe the concepts behind STORM imaging. Then we discuss the use of quantum dots and adaptive optics. Finally, comparisons and conclusions are drawn through quantitative measures using photon statistics.

Chapter 2

Stochastic Optical Reconstruction Microscopy

2.1 Background

The position of a single fluorescent emitter can be determined more accurately than the Rayleigh criteria by finding its centroid. The accuracy with which the centroid can be determined is given approximately by

$$< \Delta x >^2 = \frac{s^2}{N}, \tag{2.1}$$

where s is the width of the PSF, N is the number of photons detected and Δx is the error in localization [12]. This equation can be refined by introducing pixelation noise, or the increase in error due to the finite size, a, of the pixels in the image being taken,

$$< \Delta x >^2 = \frac{s^2 + \frac{a^2}{12}}{N}. \tag{2.2}$$

The factor $a^2/12$ is the variance of the top-hat distribution of size a. Therefore, pixelation noise increases the size of the spot.

This equation describes the fundamental principle upon which STORM is based [14]. Originally developed for particle tracking in low-density lipoprotein receptors, it was found that the center of an object can be determined arbitrarily precisely given a sufficient number of photons [15]. The localization precision depends upon two important variables, the shot noise present in the signal and the noise from the background signal. Shot noise, which scales as $N^{-1/2}$, is due to the quantized nature of light (i.e. photons) in the spot. Background noise, scaling as N^{-1}, refers to the noise created by out-of-focus light, CCD read noise, dark current, and other factors. The localization variance due to pure background noise is given as,

$$< \Delta x >^2 = \frac{4\sqrt{\pi} s^3 b^2}{aN^2}. \tag{2.3}$$

Where b is the standard deviation of the background noise of the system. Combining the background and pixelation noise finally gives,

$$< \Delta x >^2 = \frac{s^2 + \frac{a^2}{12}}{N} + \frac{4\sqrt{\pi} s^3 b^2}{aN^2}. \tag{2.4}$$

So at low light levels it becomes essential to minimize the background noise present to ensure high precision [14].

It has already been shown that the location of one dye molecule can be determined with an accuracy of 1.5 nm in an experiment in which Myosin V was labeled with a single bifunctional rhodamine or monofunctional Cy3 molecule. The step size of Myosin V moving along F-actin filaments affixed to a coverslip was then measured using total internal reflection fluorescence microscopy [16]. Fluorescence imaging with one-nanometer accuracy (FIONA) was over a 200-fold improvement in the localization accuracy of single fluorophores using wide-field methods at the

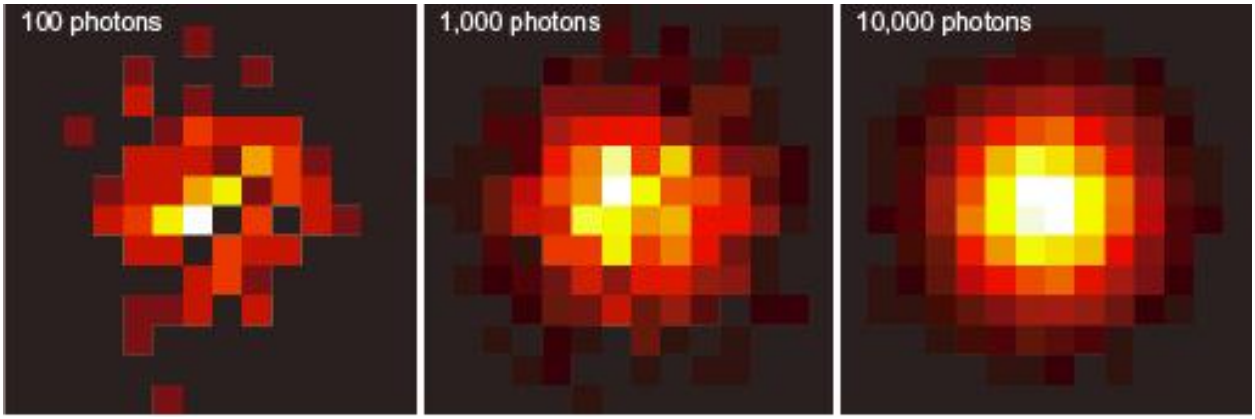

Figure 2.1: A visual representation of resolution as a result of the equation found by Webb et al. Observe the increase in localization accuracy as the photon count increases.

time of its creation. By collecting a sufficient number of photons, they were able to localize the image (a point spread function) to a Gaussian function using Equation 2.4 [14].

However, this precision localization does not translate directly to image resolution. Imaging a single molecule doesn't create an image. To create an image many molecules must be detected. Overlapping PSFs cause erroneous localization results. Methods have been developed, such as stochastic blinking, to circumvent this limitation by only having one active point within a diffraction limited area [17].

2.1.1 Stochastic Localization Methods

In 2006, three papers introduced a general technique for solving the problem of overlapping point spread functions (stochastic framework measuring a number of emitted photons) independently: PALM [12], STORM [11], and FPALM [13].

At the base of this approach is the stochastic switching, or blinking, of fluorophores. While overlapping PSFs from multiple emitting fluorophores prevents determining the centroid of the emission, this can be overcome by turning on only one of the fluorophores. Repeating this step for

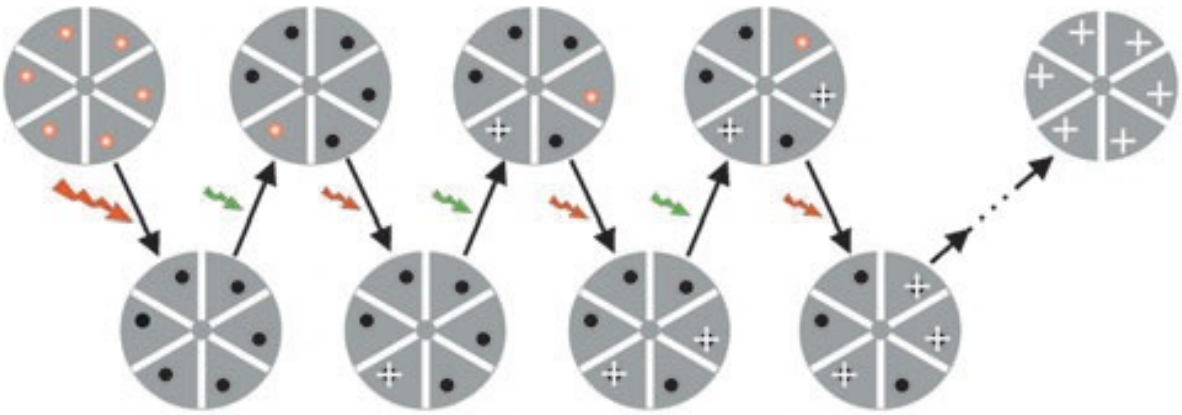

Figure 2.2: An example of photoswitching being used for STORM on a hypothetical 6 point diffraction limited object. All fluorophores are first switched to a dark state using a strong red laser. Then, a weaker green laser is pulsed so that a random and sparse set is activated. The position is recorded and these steps are continued until all points are accounted for [11].

every fluorophore allows each fluorophore to be localized. While the example given is controlled, the blinking in actual samples is random. This accounts for the large image sets required to randomly activate subsets of fluorophores so that individual fluorophores may be localized over time. Only a small number of active points emit in a single exposure. The following subsections outline the minor differences in the three techniques.

2.1.2 PALM

In ref. [12], the photoactivatable fluorescent protein, Kaede, is used to produce resolutions of approximately 20 nm in a COS-7 cell expressing the lysosomal transmembrane protein CD63. A 405 nm wavelength of light, pulsed once, activates only a sparse set of Kaede proteins which are then localized. The photon statistics can be seen in Figure 2.3. Active points are recorded and then subsequently bleached. The laser is then pulsed again to activate a new subset. Verification came

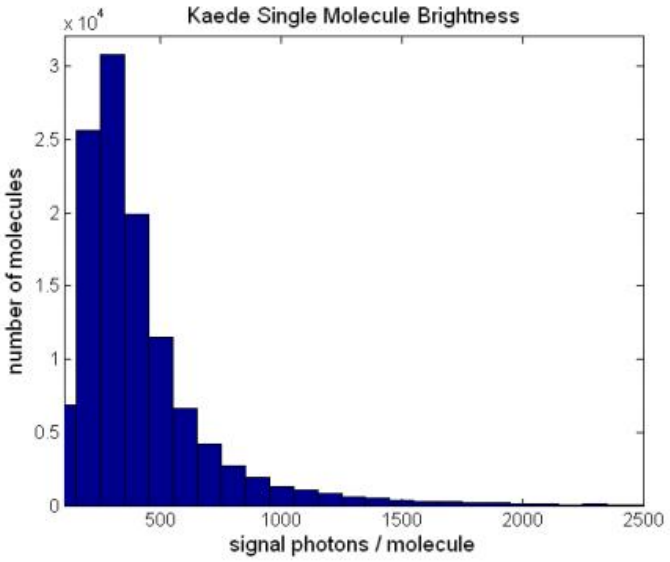

Figure 2.3: Histogram of photons detected per cycle for Kaede.

by overlaying the captured STORM image over a transmission electron microscopy (TEM) image. TEM can image resolutions as low as 0.2 nm [18], providing a sufficient scale to judge STORM.

2.1.3 FPALM

Hess created FPALM using the same technique found in PALM. Photoactivatable fluorescent proteins are continuously illuminated by the readout light, in their case an Ar+ ion laser. Then an activation light is pulsed, turning on a sparse subset of molecules. Active molecules are imaged until they spontaneously photobleach or become non-fluorescent which results in $\sim$86 nm of spatial resolution. One minor difference is that FPALM made use of photoactivatable green fluorescence protein (PA-GFP), whereas PALM used Kaede as a molecular marker [13].

2.1.4 STORM

STORM, again, relies on the same underlying principle of sequentially activating small stochastic numbers of markers in which there is no overlap in a diffraction limited area [11]. However, the marker used in this experiment was a photoswitchable fluorophore, in this case Cy3-Cy5 (i.e. an organic fluorophore, not a protein). Differing wavelengths were used to turn the fluorescence on and off like a switch, hence the term photoswitching, seen in Figure 2.2. A red laser, 633 nm, is used to switch Cy5 to the dark state. A green laser, 532 nm, is used to return Cy5 to the fluorescent state. This experimental setup acquired images with a resolution of 20-30 nm and observed on average 3,000 photons per switching cycle. The specific action of the various markers are examined with more detail in Section 3.1, along with variations that use one laser instead of multiple. For consistency throughout this paper, STORM will be used to designate all types of single molecule localization microscopy.

2.2 TIRF and 3DSTORM

In most STORM experiments total internal reflection fluorescence (TIRF) is utilized [19]. TIRF microscopy only illuminates the first $\sim$100-200 nm below the coverslip, eliminating much of the background light and thus increasing localization precision. TIRF accomplishes such shallow excitation by the use of evanescent waves. When incident light is reflected off a medium (e.g. a glass coverslip) at greater than the critical angle, 100% reflection occurs. An evanescent wave is created on the other side of the interface. These waves exist because magnetic and electric fields cannot be discontinuous at a boundary. TIRF, however, is not necessary to perform STORM. In fact it is useless when attempting to reconstruct 3D images thicker than a few hundred nanometers.

Three-dimensional fluorescence imaging is most commonly performed using confocal or multi-photon microscopy, the axial resolution of which is typically in the range of 500 - 800 nm, three times worse than the lateral resolution [20, 21]. Axial resolution may be improved to 100 nm

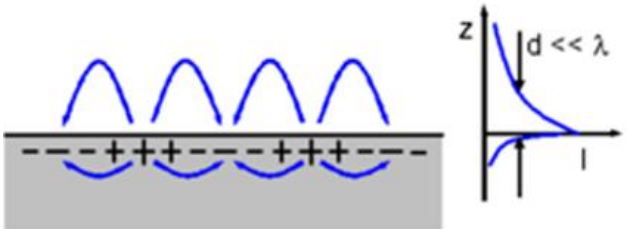

Figure 2.4: Demonstration of evanescent waves created when light is completely reflected. The graph to the right visualizes the exponential dependence of the electromagnetic field intensity on the distance away from the interface.

by 4Pi [22] and I^5M [23] microscopy. Even more impressive, axial resolutions of 30-50 nm have been attained by pairing STED with 4Pi illumination geometry, but this setup does not provide high resolution in lateral dimensions (under 80 nm) [24]. The original papers on STORM created two dimensional images of the fluorophores at the coverslip. To provide depth information, additional methods must be used. A few of the more successful techniques are described in the following subsections.

2.2.1 Biplane Fluorescence Photoactivation Localization Microscopy

Biplane fluorescence photoactivation localization microscopy (BPFPALM) images two different objective planes of a sample at the same time [25]. This is accomplished by inserting a beam splitter cube prior to the CCD. One path is directed straight into the CCD, labeled the transmitted (shorter) path. The other longer pathway reflects off a mirror and is imaged as if the sample was 350 nm closer to the objective than the original objective plane. Signal from the two recorded regions of interests can then be combined into a 3D raw data stack consisting of two planes.

Feasibility was tested by imaging caged fluorescein bound to antibodies on a coverslip embedded in 87% glycerol. The stack is fit to a 3D Gaussian to localize the particle (i.e. an x, y, z voxel). Voxel intensities were assigned by adding all detected photons within that voxel. They measured a

full width at half maximum (FWHM) of 75 nm axially while retaining 30 nm of resolution laterally. Experimentally obtained 3D PSF's were measured by independently imaging a small fluorescent bead as a function of the z-dimension position of the sample relative to the objective.

2.2.2 Astigmatic PSF

Astigmatism can be introduced with a cylindrical lens. Introducing astigmatism into the PSF provides axial information because it creates a focus offset between the two lateral directions. Not only will the localizations carry x and y information, but from the severity and direction of ellipticity, a z coordinate can also be calculated. Referencing Figure 2.5, a bead will have marginal x and y focus at 0 depth. However, as the depth changes positively there will be a focusing of y. Conversely as the depth moves negatively there will be a focusing of x. This technique was first introduced in 1994 when it was used to track individual particles in directed and diffusive motions [26]. By placing the cylindrical lens into the beam path instantaneous axial information may be observed from each individual image enabling live 3D cell imaging [27]. Holtzer et al. yielded 25 nm in both x and y and 67 nm in z. 3DSTORM presents a method that exhibits superresolution in three dimensions while keeping the cost and complexity very low.

Huang et al. made use of this method in 2008 paired with STORM. They stained mitochondria and microtubules in mammalian cells in an attempt to map the spatial relationship between the two. Tom20 and β-tubulin were both stained for two-color 3D STORM. A405-Cy5 labeled secondary antibodies detected mitochondria, whereas A555-Cy5 or A488-Cy5 labeled the microtubules. An alternating sequence of 405 nm and 532 nm laser pulses activate the respective probes. Then a 657 nm laser in between the aforementioned pulses localized the activated fluorophores. Localizations were colored in correspondence with the activation laser immediately preceding the event [28].

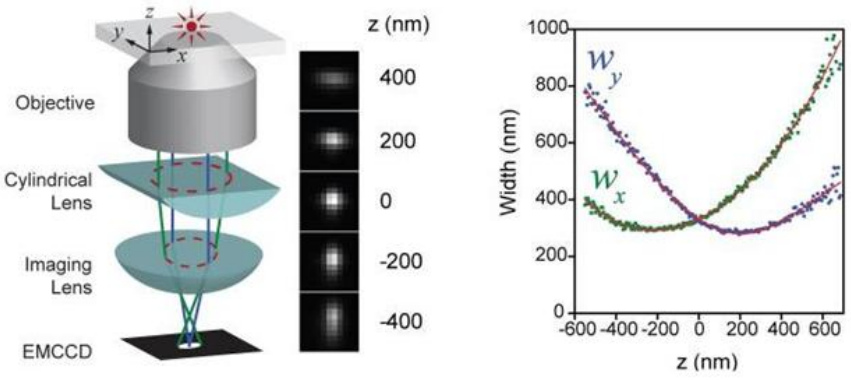

Figure 2.5: **(Left)** The optical setup on the left describes the method of determining z coordinates from the ellipticity of its image. Introducing a cylindrical lens causes the resolution in x and y to become independent of one another. Therefore, the more unresolved a particle is in the x direction, the more positive its z position. Conversely, the more unresolved the particle's y direction corresponds to a more negative z position. **(Right)** A calibration curve of image widths w_x and w_y as a function of z [24].

2.2.3 Double-Helix PSF

The axial position can be determined more accurately using a double-helix PSF (DH-PSF) [29]. A DH-PSF produces an image of a point-source that is two points rotating around each other as shown in Figure 2.6. Creating a DH-PSF requires the addition of an achromatic lens placed at a distance f from the microscope's image plane. This produces the Fourier transform of the image (i.e. the back pupil plane) at a distance f behind the lens. The phase of the Fourier transform is then modulated by reflection from a liquid crystal spatial light modulator (SLM), a device that allows for control of the amplitude and phase. In this case the SLM is adjusted to create a DH-PSF in the image plane. Reflecting the beam off of the SLM causes a multiplication between the Fourier transform of the sample image and the DH-PSF transfer function. Equivalently, every point is convolved with two DH-PSF lobes, with the angular orientation of the lobes dependent upon the axial location.

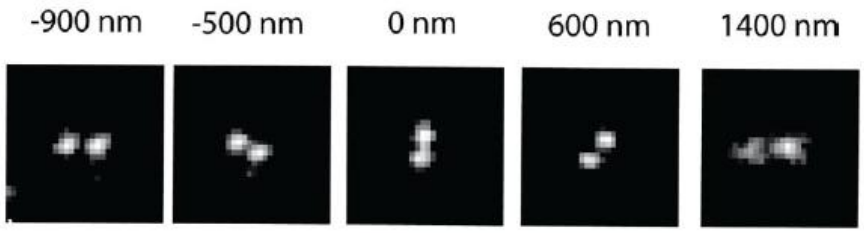

Figure 2.6: Images of a fluorescent bead used to calibrate the system for depth based on lobe location. 0 nm is set as the focus [29].

Theoretically the DH-PSF provides more accurate 3D localization then the astigmatic PSF [30]. Unfortunately, this method loses a lot of power due to the insertion of the SLM. Also, it creates a fair amount of background noise when compared to the other techniques. Despite this, DH-PSF localized a single molecule within 10-20 nm in all three dimensions.

2.2.4 Interferometric Photoactivated Localization Microscopy

Interferometric photoactivated localization microscopy (iPALM) places two objectives above and below the sample, which is placed in between two glass coverslips [31]. An emitted photon can simultaneously travel two distinct optical paths, which can then be subsequently recombined so that the photon interferes with itself. Based on the z position of the fluorophore, the photon will travel a shorter or longer path when either emitting toward the bottom or top objective. The phase difference between these two paths may then be measured and correlated to depth. Figure 2.7 demonstrates two microtubules crossing within 70 nm of each other axially. The FWHM of each microtubule is 25-30 nm, which is in agreement with microtubule dimensions.

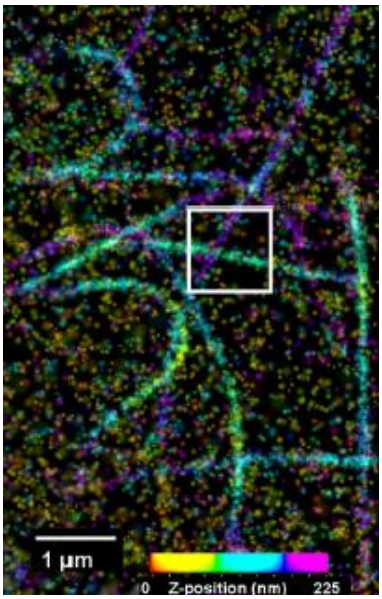

Figure 2.7: iPALM image of microtubules in PtK1 cell expressing human α-tubulin fused to *m*-KikGR with z axis color-coding. The region of interest demonstrates overlapping tubules [31].

2.3 Deep Tissue Imaging

Biological tissue is opaque and scatters light effectively. This causes the image quality to degrade with depth rapidly in thicker samples. For instance, conventional confocal microscopy is limited to only a few hundred microns of imaging into the sample. Fruitfly larvae or tissue slices may be several times that. It also becomes increasingly important to view the sample *in toto* to obtain global information. There exist techniques outside of microscopy, such as magnetic resonance imaging (MRI) for imaging large samples, but these lack needed resolution [32]. Two techniques that have shown promise are light sheet microscopy and optical projection tomography (OPT). Light sheet microscopy can image as deep as a few millimeters and has been applied to small organisms. OPT, however, can go up to 10 mm by taking a series of images from varying angles.

Both, again, lack the resolution gains found in sub-diffraction microscopy. Combining STORM and light sheet microscopy led to individual molecule localization-selective plane illumination

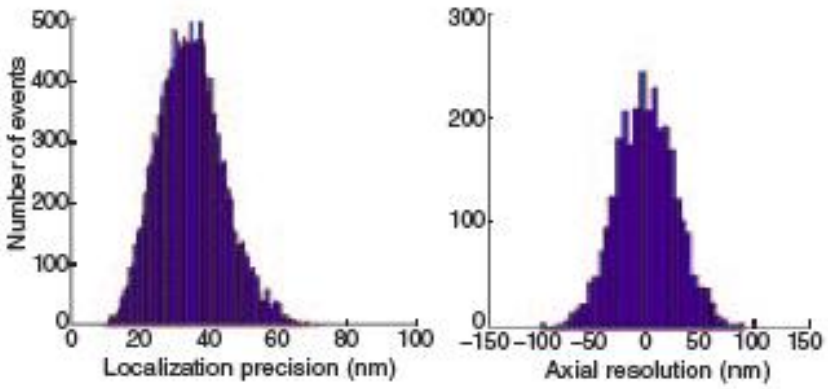

Figure 2.8: **(Left)** Spatial resolution as a result of IML-SPIM, which was found to be less than 35 nm. **(Right)** Axial resolution was much more reliant on sample characteristics and displayed a range 65-140 nm [33].

microscopy (IML-SPIM) [33]. Taking advantage of confined illumination approaches reduces photobleaching, and increases the signal-to-noise ratio and capability to image thick biological samples when compared to wide-field fluorescence microscopy. Still, this technique only boasts resolutions of 35 nm spatially and 65-140 nm axially (Figure 2.8). Adaptive optics, originally used in astronomy, is finding use in microscopy techniques when viewing thick samples. This is examined more in Chapter 5.

2.4 Final Image

Before STORM raw data is captured, it is important to sample the focal plane with respect to the Nyquist Criterion. Due to a microscope being diffraction limited at $\sim$200 nm, the system must sample at twice this frequency (i.e. each pixel in an image must be less than half 200 nm). In our system, one pixel represents 90 nm of real space. Molecules are then pushed into an active state by a laser. Each frame has individual points of intensity that reflect the stochastically excited

fluorophores at the time the image was captured. Thresholds are then used to determine which points of intensity represent signal and not background. Once fluorophores are labeled correctly, their signal is fitted to a 2D Gaussian distribution. The signal-to-noise ratio resolves how well a Gaussian can fit the signal. This takes the blurred image and creates a best estimate where the center of each fluorophores is located [34]. As the molecules photobleach or return to a non-fluorescent state the entire process begins again. Each center is then placed in an expanding list which contains particle information regarding spatial information as well as intensity. The final image is a compilation of data from an image stack that usually contains thousands to hundreds of thousands of image frames and similar numbers of localization events. With the increased resolution it is necessary to create an image with a higher pixel count (e.g. what was once 1 pixel representing 90 nm would become 10 pixels representing 90 nm).

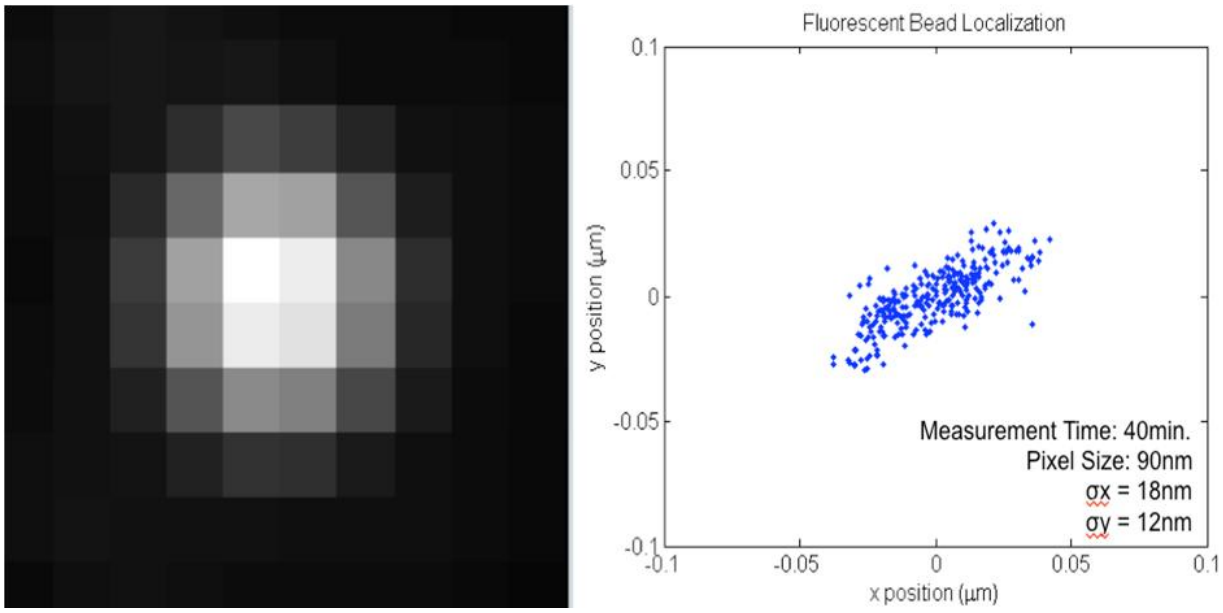

Figure 2.9: **(Left)** An image of a fluorescent bead using conventional widefield techniques. This data is taken from our system. The bead is imaged once ever 30 seconds over a 40 minute time period. **(Right)** Localizations of the bead in 2D space. This plot gives two important pieces of information. First, that the PSF moves less than one pixel over the course of 40 minutes, making drift negligible. Second, that even though the PSF seems stationary when viewing the widefield images, sub-diffraction imaging shows there is a fair amount of movement.

2.4.1 Particle Drift

To localize each molecule accurately, any drift in the position of the sample must be corrected. The image stacks are captured over an extended period of time, and with the stacks reaching sizes on the order of ten thousand, it is necessary to use appropriate methods to correct the movement. If the drift is not taken into consideration, intensity points become smeared lines and image resolution deteriorates. Mechanical and thermal drift are both corrected in any STORM image [12, 11, 35], but all of their correction is done in the post processing phase (after the images have been taken).

One method to correct drift is to track the motion of several fluorescent beads and then apply a fitting algorithm to the subsequent data. These beads serve as fiducial marks. As they drift over the entire stack of images, the average motion of these select beads is subtracted from the coordinates of the whole which yields a final drift-corrected image. What was once a very skewed and broad point, as seen in Figure 2.9, became a narrow PSF with a full width at half-maximum of 18 ± 2 nm.

Another approach to drift correction was used in STORM on Drosophila mitotic chromosomes labeled with H2AvD-EGFP, a histone H2A variant [35]. To estimate and correct mechanical drift, they use a correction image stained with DAPI, 4',6-diamidino-2-phenylindole, that is denoised and passed through a Mexican-hat and Wiener-type high-pass filter. The contrast transfer function is a Gaussian distribution. This image is then cross-correlated with a reference image treated in a similar way. Lateral movement is then recorded between the two and the movement over time smoothed using a low-pass Gaussian filter. Drift between their STORM images is then interpolated and corrected for by shifting the axis [35].

Chapter 3

Fluorescent Tagging of Proteins for STORM

3.1 Fluorescent Probes

Many fluorophores exist, but for use in single molecule localization, the fluorescent probes must be capable of being photoactivated, photoconverted, or photoswitched by a specific wavelength of light. Other attributes that should be taken into account are the brightness and contrast levels which directly correlate with the image resolution. Brightness is the product of the fluorescence quantum yield (φ) and the molar extinction coefficient (ε_{abs}) [36],

$$\text{Brightness} = \varepsilon_{abs} * \varphi. \tag{3.1}$$

As stated, the more photons emitted and detected, the higher the resolution will be.

Fluorophores for use in STORM can be divided into fluorescent proteins and molecular dyes. Green fluorescence protein (GFP) was one of the first fluorescent proteins developed and is the most widely used, even to this day. It is a 29.6kDa protein that, when exposed to blue light (488 nm) emits a bright green fluorescence [37]. GFP, like all new fluorescent proteins, exhibits an advantageous property of not being phototoxic when tagged to living cells. Synthetic derivatives have

since been created to exhibit higher quantum yields and thus, brightness. Despite this, however, GFP is not considered a good candidate for STORM imaging. When engineered into a photoactivatable version (PA-GFP), it only has 8-41% of its original brightness [36]. In fact, the original paper by Betzig [12] used PA-GFP initially but opted for other fluorescent proteins (tetrameric Kaede and various oligomers of EosFP) due to their higher brightness [12]. Some optical highlighters can be turned off and on like a switch using different excitation wavelengths of light. These molecules are referred to as photoswitchable dyes.

Cyanine dyes, used in a pair of Cy3-Cy5, can be turned on and off for hundreds of cycles before permanent photobleaching. A red laser at 633 nm and $30^{W}/_{cm^2}$ pushes the Cy5 from an excited state to a stable dark state. Then a green laser, 532 nm and $1^{W}/_{cm^2}$, converts the Cy5 back to a fluorescent state [11]. The rate of conversion back to the fluorescent state is based on the secondary effector, Cy3, and how closely it is tagged to Cy5. These photoswitchable fluorescent probes can be switched on and off so that only a sparse subset of molecules are activated. Only a small fraction ($\ll$1 part in 100) is activate at a time [36].

3.2 Photoswitching of Organic Fluorophores

Paired fluorescent probes, while viable, lead to a much more complicated optical and chemical platform requiring multiple lasers to excite them and more involved chemistry. There is another way to acquire a sparse data set using the photoswitching of non-paired standard organic fluorophores and a single excitation laser. All fluorophores have a triplet state that can be used to switch off fluorophores in order to create STORM images [38]. Excited molecules can transfer to a triplet state which has a very long lifetime because relaxation to the ground state via a "dipole allowed" photon emission is not allowed. The triplet state is a non-fluorescent pathway that allows a fluorophore to return to the ground state without emitting a photon.

Ground state depletion microscopy (GSDM) [39] uses the triplet state to its advantage to achieve subdiffraction resolution. Dyes that exhibit this type of behavior, with a longer dark state than on-state, are used as an alternative platform to photoswitching microscopy. An illuminated spot is surrounded by a donut shaped illumination source that is of a longer wavelength which pushes surrounding fluorophores into a triple state. This technique is very similar to STED, described in Figure 1.5. This arrangement produces a PSF that is 4 times smaller than confocal microscopy. Microtubular strands at distances $<$80 nm can be resolved.

Direct stochastic optical reconstruction microscopy (dSTORM) [38, 40] is another method which acquires STORM images by exploiting non-radiative pathways, but only uses one laser. From a simplicity standpoint, dSTORM is far ahead of other techniques so far mentioned. Resolution is not sacrificed for this setup. When viewing fluorescent probes on a coverslip, a 21 $\pm$ 2 nm of axial resolution can be recorded. Using probes on microtubule filaments measures an apparent width of 30-50 nm, which is close to the expected value of 25 nm.

dSTORM takes advantage of organic fluorophores, within the rhodamine and oxazine dye classes, that exhibit this triple state. These dyes are photoreduced in the presence of potent electron donors such as aromatic amines (i.e. upon contact or collision with aromatic amines the electronically excited fluorophore will be reduced).

3.2.1 Simplified Rate Equation Model

A simple jablonski diagram of a molecule with only one non-radiative pathway is shown in Figure 3.1. This model provides the mechanism upon which dSTORM is based.

$$\frac{\partial N_0}{\partial t} = -(\frac{I\sigma}{t\omega})N_0 + \frac{N_2}{\tau_1} + \frac{N_2}{\tau_3}. \tag{3.2}$$

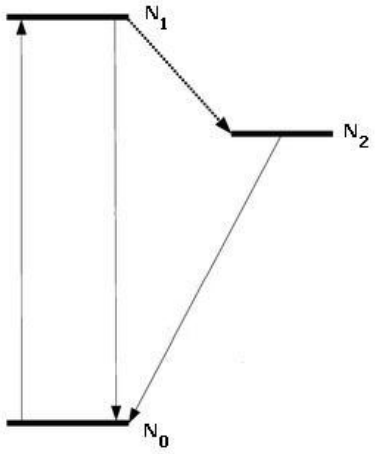

Figure 3.1: A jablonski diagram with only one non-radiative pathway.

$$\frac{\partial N_1}{\partial t} = (\frac{I\sigma}{t\omega})N_0 - \frac{N_1}{\tau_1} - \frac{N_1}{\tau_2}. \tag{3.3}$$

$$\frac{\partial N_2}{\partial t} = \frac{N_1}{\tau_2} - \frac{N_2}{\tau_3}. \tag{3.4}$$

$\tau_0 \equiv \frac{I\sigma}{t\omega}$ is the excitation rate to excited state. σ represents the absorption cross-section (cm^3) of a molecule and is related to ε_{abs} by units $[\frac{1}{M*cm}]$.

$$\sigma = 1000 * \ln(10)\frac{\varepsilon}{NA} \tag{3.5}$$

τ_1 is the lifetime of the excited state (radiative decay). τ_2 represents the intersystem crossing rate, and τ_3 is the lifetime of the triplet state ($\tau_3 \gg \tau_1$). The population of molecules is conserved and normalized to 1 so that $N_0 + N_1 + N_2 = 1$. In the steady state, all time derivatives simplify to 0. Finding N_0, N_1, N_2 from the above equations respectively

$$\frac{N_0}{\tau_0} - \frac{N_1}{\tau_1} - \frac{N_1}{\tau_2} = 0, \tag{3.6}$$

$$\frac{N_1}{\tau_2} - \frac{N_2}{\tau_3} = 0 \Rightarrow N_2 = \frac{\tau_3}{\tau_2} N_1, \tag{3.7}$$

$$N_0 = 1 - N_1 - N_2. \tag{3.8}$$

Multiplying Equation (3.8) through by $\frac{1}{\tau_0}$ gives

$$\frac{N_0}{\tau_0} = \frac{1}{\tau_0} - \frac{N_1}{\tau_0} - \frac{N_2}{\tau_0}. \tag{3.9}$$

Substitute this back into Equation (3.6) and simplify

$$\frac{1}{\tau_0} - \frac{N_1}{\tau_0} - \frac{N_2}{\tau_0} - \frac{N_1}{\tau_1} - \frac{N_1}{\tau_2} = 0 \tag{3.10}$$

$$(\frac{1}{\tau_0} + \frac{1}{\tau_1} + \frac{1}{\tau_2})N_1 + \frac{1}{\tau_0}\frac{\tau_3}{\tau_2}N_1 = \frac{1}{\tau_0} \tag{3.11}$$

$$N_1 = \frac{1}{1 + \frac{\tau_3}{\tau_2} + \tau_0(\frac{1}{\tau_1} + \frac{1}{\tau_2})} \tag{3.12}$$

Equation (3.12) may then be represented in either no light, or lots of light scenarios. Given no light $\tau_0 \to \infty$ and $N_1 \to 0$. With lots of light $\tau_0 \to 0$ and $N_1 = \frac{1}{1+\frac{\tau_3}{\tau_2}}$ and $N_2 = \frac{1}{1+\frac{\tau_2}{\tau_3}}$. Therefore, if $\tau_3 \gg \tau_2$ then only a small fraction of molecules are active.

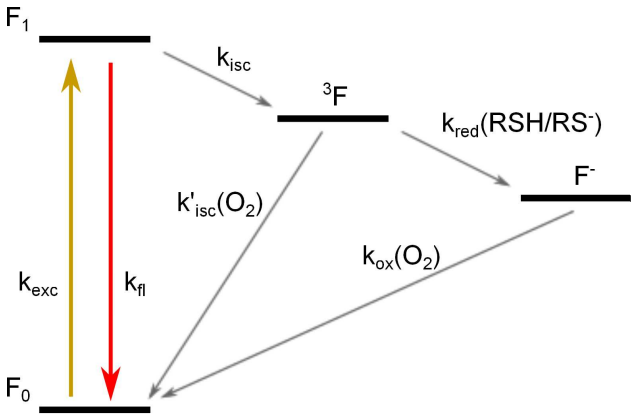

Figure 3.2: This diagram illustrates the reaction mechanism. Dye is excited with rate k_{exc} which leads it to then fluoresce with rate k_a or enter the triplet state ^3F. Rate for entering this triplet state is determined by an intersystem crossing rate k_{isc}. The triplet state may then react with oxygen to repopulate the singlet ground state (F_0), or react with the thiol at rate k_{red} to form a semi-reduced dye radical F^-. This radical may then react with oxygen to return to the ground state.

3.2.2 Thiol Mediated Blinking

The triplet state blinking discusses in the last section can be improved upon by putting the molecules into a long-lived non-radiative charged state. Then the photoswitching behavior of organic dyes can be controlled with the chemistry of the mounting solution. Adding thiols (sulfur groups) can increase the time dyes spend in a non-radiative state by producing more non-fluorescing pathways, seen in Figure 3.2. Thiols are considered a weaker electron donor. Addition of these thiols has a negligible affect on quenching the excited singlet state. Due to this, the triplet state is also quenched by millimolar concentrations of a thiol like monoethanolamine (MEA) or β-mercaptoethanol (BME). This reduction produces a corresponding dye radical anion and thiyl radical. Rhodamine radical anions can last for several hundred milliseconds in the presence of oxygen which allows us to create the desired sparse dataset [41]. Dr. Markus Sauer's group laid the ground work that single molecules could blink up to 100 times in an environment using MEA as a thiol to facilitate a redox reaction [38].

Redox couples exist in cells innately, the most abundant being the glutathione disulfide-glutathione (GSH/GSSG) couple. Concentration in cytosol has been reported as 1-11mM which of course can vary based on cell line and structure being observed. This allows dSTORM to occur in living cells. These pathways can be modified and controlled using a buffer system termed ROXS (reducing and oxidizing system) [42]. Furthermore, the rate at which fluorophores are pushed into the dark state may be tuned. Reduction of the triplet state by MEA and oxidation of the intermediate reduced state by oxygen are facilitated by irradiation. Therefore laser intensity has a direct relationship to fluorophores entering a non-fluorescent pathway (i.e. higher intensity leads to more fluorophores pushed into the triplet state).

Various dye classes, however, react differently in the presence of oxygen. For instance, carbocyanine dyes (e.g. Dy505, Alexa Fluor 488, ATTO 532) are oxidized rapidly. This makes it important to remove oxygen so that the photostability increases. It also acts to stabilize the off state, making it last longer. Buffers used with carbocyanine dyes will typically have some form of oxygen scavenger.

Rhodamine dyes, on the other hand, are much more stable when in the presence of oxygen. It is important to note that while the dyes may return to their ground state spontaneously, oxidation also returns the molecules to their ground state. Oxygen presence is therefore a necessity for blinking. Without it a radical anion can be stuck in a non-fluorescent state for hours. With intersystem crossing yields of 0.2-1%, single rhodamine dyes will at best emit 500 photons before being reduced (25-50 detected photons) [42]. So without sufficient oxygen, the molecules would eventually all become stuck in a non-fluorescent state giving the illusion that they have photobleached.

Short wavelength light helps remove fluorophores trapped in the dark state. There have been prior experiments showing that irradiation by shorter wavelength light after “bleaching” serves to re-energize the fluorophore [43]. While these studies do not specifically go into the conformational changes occurring within the molecule, the research they are based on does. E2GFP will be used as an example of this change in chemistry. Photochromism, a trait these fluorophores demonstrate,

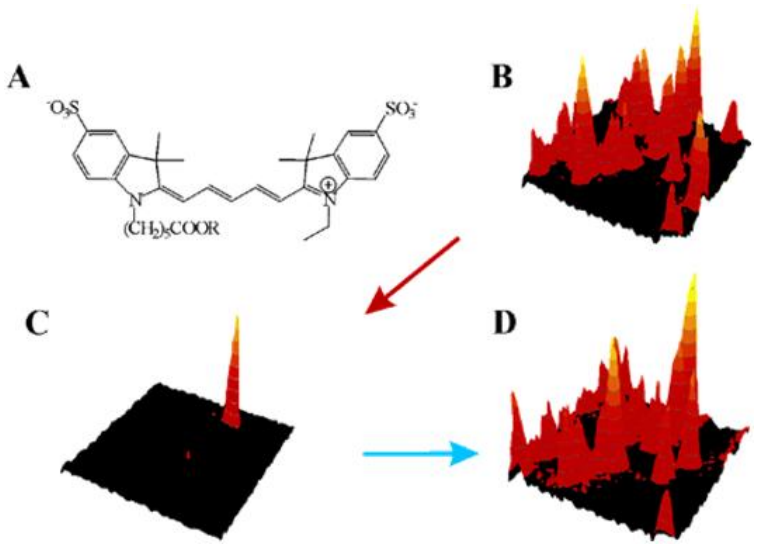

Figure 3.3: **(a)** Molecular structure of carbocyanine dye Cy5.**(b)** Fluorescence scanning image of Cy5-labeled dsDNA in PBS at a wavelength of 633 nm.**(c)** Fluorescence image (excitation at 633 nm) of the same surface area showing that most Cy5 molecules are no longer in a fluorescing state after the first scan. The surface is then irradiated with a 14 $^{kW}/_{cm^2}$ 488 nm laser. **(d)** The same surface area is now again re-excited using the 633 nm laser and the Cy5 is emitting photons again. [43]

is the reversible transformation of a chemical species between molecular structures via absorption of electromagnetic radiation.

Observing the recovery spectra of E2GFP and the marked blue shift of the absorption spectra seemed to suggest that photoswitching was accompanied by protonation of the chromophore. One group studied the photophysical model for E2GFP and used *ab initio* calculations adding one by one the three possible hydrogen bonds between the neutral chromophore and the protein (Gln94 and Arg96). Each interaction resulted in the observed redshift. This analysis, however, does not uniquely identify the total photoconversion process [44].

Alternatively, the chromophore may be being converted to a different isomer, like in cis/trans photoisomerization. Configurations could then lend themselves to experiencing different energy

barriers to return to the ground state. The configuration of the chromophore in the dark state, for example, favors nonradiative decay pathways [45]. Measuring the distance between two side branches (Arg96 and Gln94) showed a sudden increase in distance between the branches. This suggests a cis/trans state does exist for the E2GFP molecule. Currently there is still no conclusive evidence as to what chemical changes occur in the molecule that enables the re-energizing with lower wavelengths. Despite the absence of a conclusive answer as to how the mechanism is taking places, this method has been used throughout the STORM community to increase the lifetime of fluorophores.

A major disadvantage for both fluorescent proteins and molecular dyes is that they irreversibly photobleach. A novel use of nanotechnology, the quantum dot (QD), can replace these fluorescent proteins and organic molecular markers. By tuning the quantum dot size (1-10 nm), these biological highlighters exhibit a wide range of fluorescence emission wavelengths. Quantum dot's quantum yield and stability are their most attractive attributes as a candidate for STORM. Bleaching time is extended to hours beyond typical fluorophores.

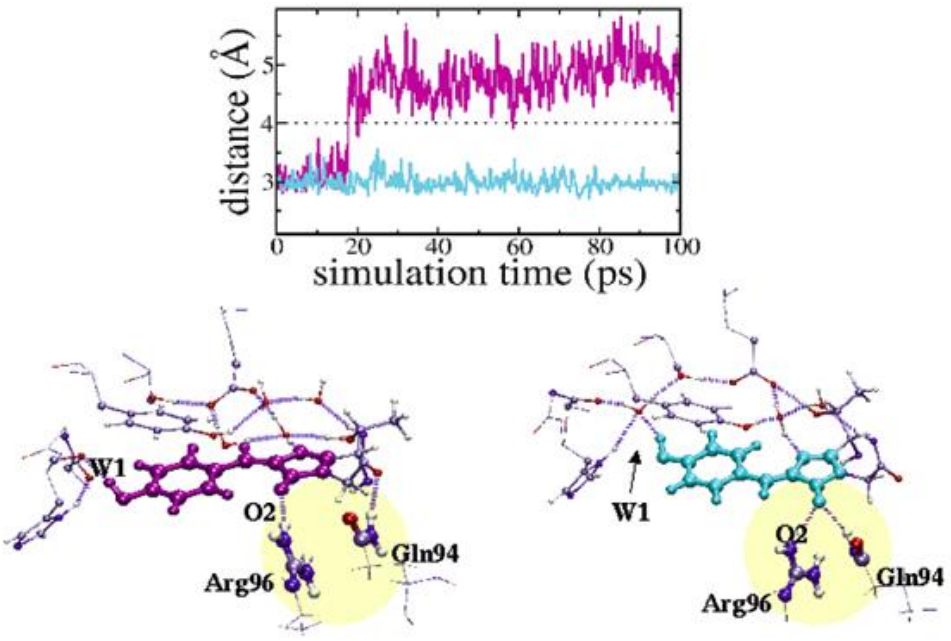

Figure 3.4: The top chart shows the distance between O2 of the chromophore and the donor of Gln94 during the first 100 ps of the simulation for the trans state (magenta) and cis state (cyan), the sudden increase in distance coming from the broken hydrogen bond. The lower two images illustrate the trans state **(left)** and the cis state **(right)** obtained from the molecular dynamics simulations.

Chapter 4

Quantum Dots

4.1 Structure

In semiconductors and insulators, there is an energy gap between the highest energy occupied states, the valence band, and the lowest energy unoccupied states, the conduction band. The bandgap is the energy range in a solid where there are no electron states, and this energy gap is referred to as the bandgap of the material. Typical semiconductor materials (Si, GaAs, CdSe, etc) have bandgap energies ranging from the near infrared to the near ultraviolet. When a narrow bandgap material is encompassed by a larger bandgap material the electrons and holes are confined to the narrow gap material and their energies are restricted to discrete quantum levels. If the dimensions of confinement are small compared to the electron wavelength (on the order of nanometers), the lowest discrete quantum state will be measurably higher in energy than the bandgap of the bulk material. When three-dimensional confinement is created with a semiconductor, it is known as a quantum dot [46].

Quantum dots are nanoparticle semiconductors, and due to their discrete energy states can be considered as artificial atoms. Conveniently, quantum dots can be optically excited. When a photon is absorbed, electrons in the QD gain energy leading to the creation of excitons. An exciton is a

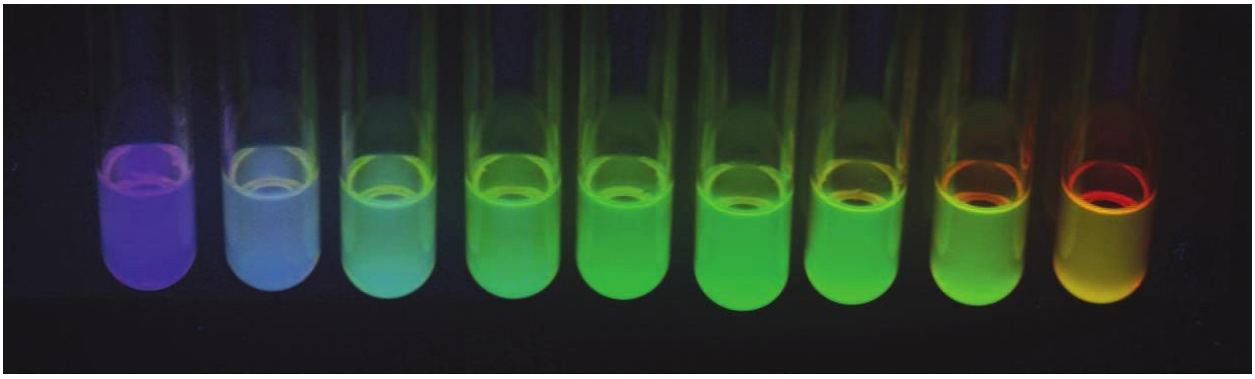

Figure 4.1: Colloidal suspensions of CdSe quantum dots with increasing size from left (approximately 1.8 nm in diameter) to right (approximately 4.0 nm in diameter).[47]

bound state of an electron and a hole. The hole is the space in the valence band left vacant by the electron and behaves like a particle with positive charge. Upon relaxation the electron returns to its lower energy state and recombines with the hole, emitting a photon. This process of optical excitation, relaxation of the excited state, and recombination is called photoluminescence (PL). The PL spectrum describes the number of photons emitted as a function of energy [48, 49, 50]. This optical behavior of quantum dots is similar to that of the organic fluorophores used in fluorescence microscopy, and quantum dots can be used as fluorescent markers in biological imaging [49, 51, 52].

These biological highlighters exhibit a wide range of fluorescence emission wavelengths. Because the degree of electron confinement changes its energy, the photon emission wavelength is controlled by the QD size, illustrated in Figure 4.2. Furthermore, their emission peaks are almost completely Gaussian and lack the "shoulders" typically displayed by other organic dyes [53]. Their broad, size-dependent PL spectra makes it possible to excite the QDs far from their emission spectra, efficiently avoiding background scattering.

However, despite these advantages the solution for using QDs in an experiment has been somewhat individual in nature. QDs do not act like molecules but as nanocolloids (another nanoparticle

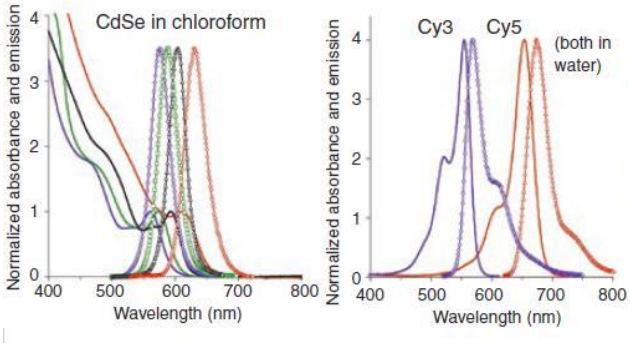

Figure 4.2: Absorption is marked by solid lines and emission by symbols. It becomes clear that QD's have a much wider absorption spectra while retaining a more narrow emission spectra [54].

that has dye molecules trapped between liquid crystals) which makes it more difficult to utilize them in biological environments [54]. Also, as semiconductors, the material within them is usually toxic requiring inert coatings. These aspects can all be remedied in some way. The major limiting factor for QDs as a biological marker in microscopy is the uncontrolled blinking.

4.2 Quantum Dot Blinking

A seemingly favorable characteristic of QDs for STORM is that their PL may feature large intensity fluctuations, known as blinking [55]. This blinking occurs on many different time scales though, making it unsuitable for STORM. Viewing the system in a purely statistical manner provides possibilities for using other algorithms in an attempt to separate emitters spatially.

Assuming that each emitter's blinking process is statistically independent, information about each individual QD is encoded in the form of its temporal intensity fluctuations. A separation technique based on Independent Component Analysis (ICA) gives the ability to accurately localize two point emitters [55]. The technique requires:

- Temporal fluctuations of individual QDs that can be considered independent. As the blinking is stochastic and thought to be caused by surface defects, this is true.
- The probability distributions must be non-Gaussian. QDs blinking scale can last as long as seconds. So, sampling at shorter time scales moves the temporal intensity distribution towards a bimodal distribution.
- Mixing of the sources to the detector is linear and mixing coefficients are not identical. Identical coefficients means the emitters are located in the same position and cannot be separated.
- Number of detectors is equal to or greater than number of sources. In other words, the limit of separable sources in an area is equal to the number of pixels detecting light from those sources.

Experimental results yield localization accuracies of $<$0.2 pixels which corresponds to $< \frac{\lambda}{30}$. It is important to note that this is from only two emitters within a diffraction limited area. ICA proves useful up to 4 emitters. Any more than 4 emitters in a diffraction limited area and the algorithm breaks down. STORM relies on a densely labeled sample, which makes ICA unavailable as a method of using QDs for STORM.

A method made to address specifically this issue is superresolution optical fluctuation imaging (SOFI) [56]. SOFI uses random temporal signal fluctuations from single emitters to create super-resolution images via higher order correlations of the fluctuations. In other words, if a molecule is blinking or shows fluctuations, it will appear in a final SOFI image. The resolution is improved in SOFI because the n-th order correlation is proportional to $(PSF(F))^n$ so that the correlations remove background and have a narrower FWHM than the normal intensity image. Figure 4.3 demonstrates this affect. Appendix A.1 contains the code for SOFI.

In practice SOFI can provide a factor of 2 resolution improvement fairly easily, but SOFI does have limitations. Photobleaching of dyes limits the acquisition time, making it a more suitable

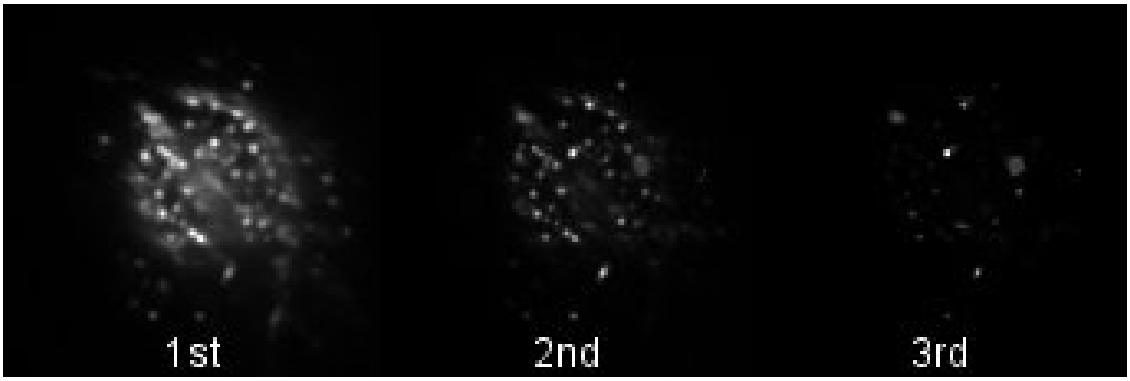

Figure 4.3: From left to right displays an image taken of *Toxoplasma gondii* with increasing orders of statistics used with SOFI. Higher orders require more blinking to be registered as a PSF.

process for QDs. Lower signal-to-noise ratios (compared to QDs) negatively affect the algorithm's performance. And finally, the typical intersystem crossing rates of conventional dyes do not fit within the window of sampling found in SOFI. This technique was specifically designed for use with QDs.

For this methodology to apply to the supperresolution imaging concept, again, it must be able to deal with arbitrarily high numbers of markers (i.e. a number of markers residing in a diffraction range as high as typically found in densely labeled samples). Due to dots spending a short time in their off state, this goal has not yet been achieved. A short lived dark state causes emitters within a diffraction limited area to overlap on the camera [57].

4.3 Blueing

One approach for using quantum dots for STORM relies upon the energy gap in QDs being strongly size dependent. This phenomenon is due to the confinement effect. Larger QDs have less confinement making the energy gap smaller. Smaller QDs have larger energy gaps. Thus, QDs made from the same material can have their emission spectra changed by altering the particles size. Large QDs

appear to be red and small QDs are blue. Colloidal QDs, which are inexpensively synthesized with wet chemistry methods, make it possible to have a specific/controlled particle size, making QDs a cheap reproducible biomarker.

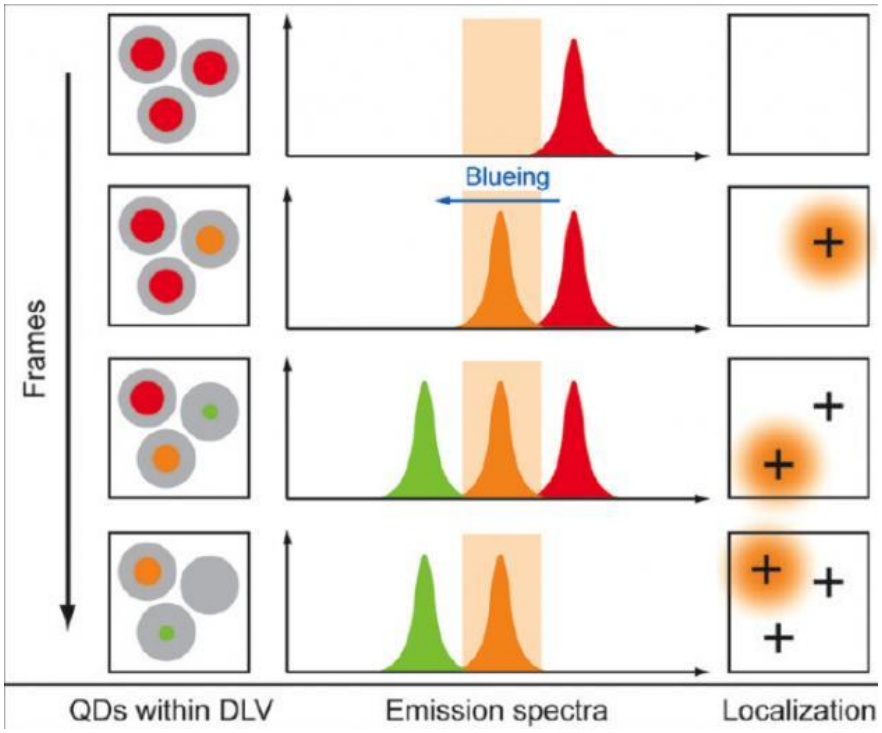

Figure 4.4: If the viewing spectra is registering only orange points, then you must start with a quantum dot in a longer wavelength. In this example red CdSe dots, within a diffraction limited volume, slowly migrate towards a shorter wavelength of light (e.g. green). As the dots stochastically shift into an orange emitting state they are registered individually. These dots continuously degrade in size until they shift back out of the viewing range, allowing a new set to be localized.

In a sample densely labeled by red CdSe QDs, QDs natively blink but do not stay in an off-state long enough for there to be a sparse dataset to build a STORM image. However, upon constant illumination, QD emission stochastically shifts toward shorter wavelengths in the presence of oxygen due to a phenomenon termed "blueing". As a result of the stochastic blueing of this sample, subclasses of QD emission wavelengths arise within the diffraction volume. The blueing process is ascribed to continuous size reduction of the CdSe core due to photooxidation. Exposure to oxygen causes the selenium surface atoms to photooxidize which creates an evaporating SeO_2 surface film,

effectively degrading the nanocrystal over time [57]. So, while the majority of the labeled sample will appear red, viewing the QDs shifting into the yellow wavelength will result in the stochastic imaging of single quantum dots.

Proving the stochastic nature of this process was done by an analysis of approximately 200 fluorescence time traces of individual photooxidized QDs [58]. Due to measured independent time lags between the initial illumination and onset of blueing for various nano-particles, the group discerned that each individual core was being photooxidized randomly. The delay was believed to be due to the migration of oxygen through the ZnS layer.

Finding alternate photoswitching mechanisms for QDs is an important area of current research. However, currently this blueing process is the only one that allows the use of QDs for STORM. And while they improve the photon statistics used for localization by orders of magnitude, they do not alleviate the issues of imaging in deeper tissue samples.

Chapter 5

Adaptive Optics

5.1 Wavefront Correction

Adaptive optics (AO) systems have been used since the 70's in astronomy. When viewing a star, the light must travel through the earth's atmosphere to a detector. While traveling, light will experience various different indices of refraction caused by pockets of temperature changes. With each change in the index of refraction the light path is slightly altered causing distortions in the wavefront, seen in Figure 5.1. These distortions directly affect image quality and signal-to-noise ratio.

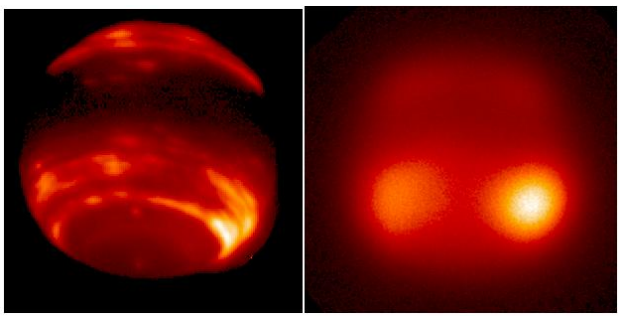

Figure 5.1: Neptune in infrared light with **(Left)** and without **(Right)** adaptive optics [59].

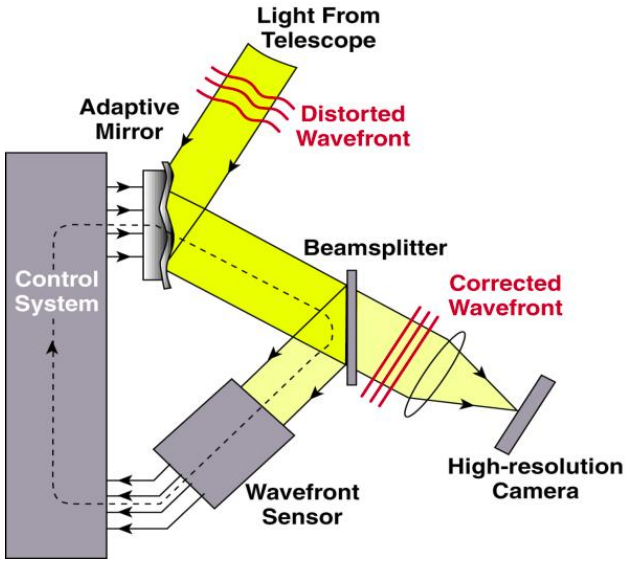

Figure 5.2: Labeled diagram of a typical adaptive optics system, demonstrating closed loop architecture [59].

These distortions can be corrected by AO. Deformable mirrors (i.e. the corrective element in an AO system) allow the user to set mechanical actuators, representing degrees of freedom, which push and pull the surface in alignment with the aberrated wavefront. Adaptive optics systems, seen in Figure 5.1, found their beginnings by way of imaging and laser beam propagation through turbulent atmospheres. These mirrors are typically used in astronomy to remove aberrations caused by light traveling through the atmosphere, rendering clear images of stars and planets. However, over the last 20 years adaptive optics has been used to image though other media such as eye fluid and biological samples. As early as 1994 a Shack-Hartmann wavefront sensor was capable of measuring aberrations in the eye [60]. Today, deformable mirrors' role in adaptive optics has made them attractive for any sort of wavefront correction, extending their use to microscopists.

When analyzing the imaging behavior of optical instruments, ray optics is the approximation for the behavior of light that is most often used. In this approximation, effects due to the wave nature of light, such as diffraction are ignored and the light field is described by vectors perpendicular

to the optical wavefront. In other words, a point source can theoretically be imaged as a point with no size instead of the Airy disk. To simplify it further is to make the paraxial approximation. This approximation assumes that all rays make a small angle with the optical axis. While this simplifies formulas, it does not accurately describe a real world optical system.

Departures from this "first-order theory" cause multiple types of aberrations. The five primary aberrations include spherical, coma, astigmatism, field curvature, and distortion [61]. Aberrations, deviations in the phase of a light beam from the ideal, occur when rays from a point source do not intersect at the image plane. Therefore, adjusting the phase of the light wavefront can correct these aberrations. This can be achieved with a deformable mirror.

In a microscope, the light beam has a circular cross section, and the aberration is described as a phase profile over a circular aperture. This phase profile is frequently described in terms of the Zernike polynomials (Figure 5.3). These Zernike polynomials are orthogonal functions that form a complete set over a unit circle so that any aberration can be described as a sum of Zernike polynomials. Using the derivatives of these polynomials can produce a gradient wave front, and thus allow for the correction of aberrations [62]. The second order of Zernike modes, Z_2^{-2} and Z_2^2, describe astigmatism. Astigmatism abberates a wavefront causing a difference in focal planes for x and y. These polynomials are of particular significance as they will be used to perform 3DSTORM.

Correction may then be carried out in a closed loop or open loop configuration. Open loop configuration measures and corrects for wavefront errors once and then proceeds with acquiring images. A closed loop system, which is used to correct rapidly changing aberrations, continuously measures and corrects the mirror while acquiring images.

5.2 Deformable Mirror

The Imagine-Eye Mirao 52E is a deformable mirror (15 mm pupil diameter) with a reflective membrane surface coated in protective silver. Fifty-two actuators push or pull the membrane up to

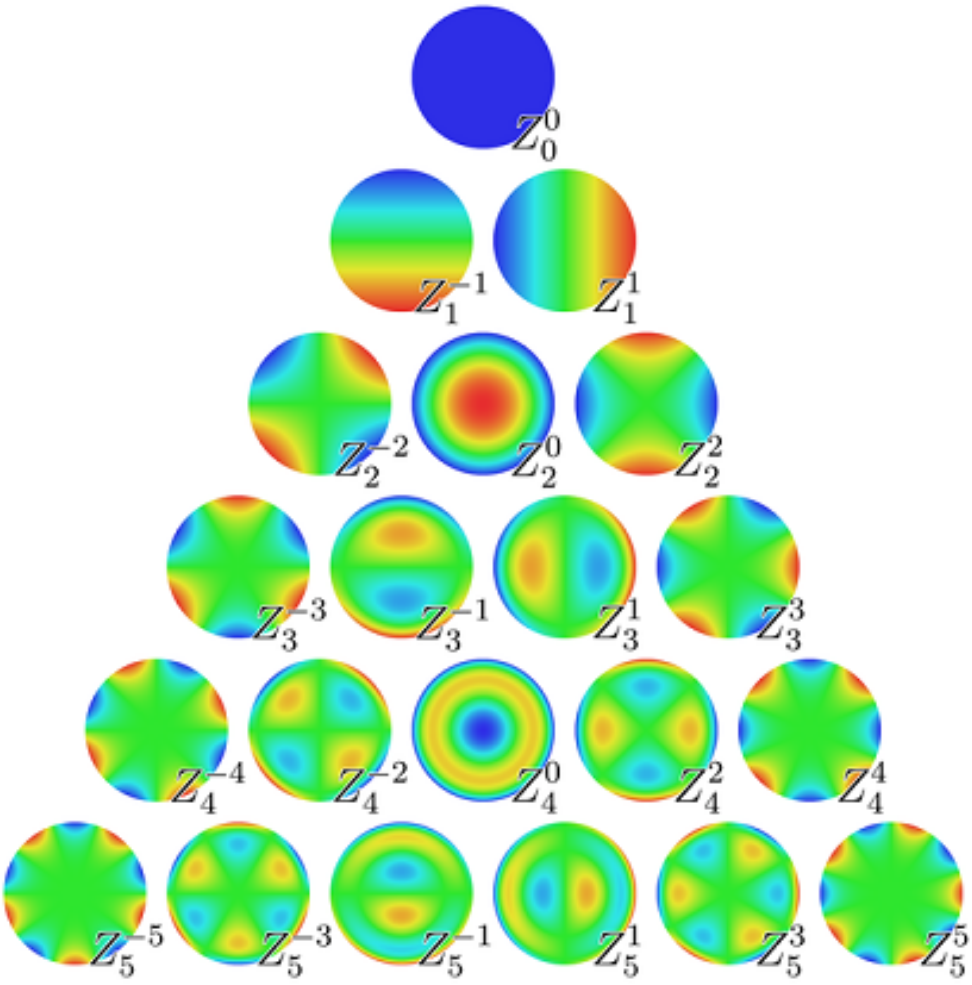

Figure 5.3: The Zernike polynomials plotted on the unit disk.

$\pm$ 50μm to create Zernike modes up to the 6^{th} order. This device enables us to correct the measured wavefront of an optical system. The behavior of the deformable mirror can be described by the matrix equation, [63]

$$H * A = W. \tag{5.1}$$

Where H is the influence function array, A is the actuator voltages array, and W is the wavefront.

To do so, first the influence function, H, must be measured. This is a N_{px} x N_{act} array where N_{px} is the number of pixels in the wavefront image and N_{act} is the number of actuators. Each column in H is the wavefront resulting from a set voltage (0.02-0.04V) being applied to one actuator. A is a N_{act} x 1 column vector and W is a N_{px} x 1 column vector. With the influence function, we now know how the system will react to step voltages applied to specific actuators. Once the phase of the wavefront is measured, the array H can be used to adjust the deformable mirror to correct for the phase of the wavefront. Equation 5.1 can be inverted using singular value decomposition to determine

$$A = (\bar{H})^{-1} W. \tag{5.2}$$

Setting the actuators with A will remove the phase W from the wavefront resulting in a flat phase. A flat wavefront will result in an ideal PSF at the image plane.

5.2.1 Correcting the PSF

To measure the wavefront we will use the phase retrieval technique. When viewing an image with a CCD only intensity values are recorded. This is a problem because the wavefront is determined by the phase of the light. We will use a variation of the Gerchberg-Saxton algorithm to determine the phase from intensity measurements on multiple image planes.

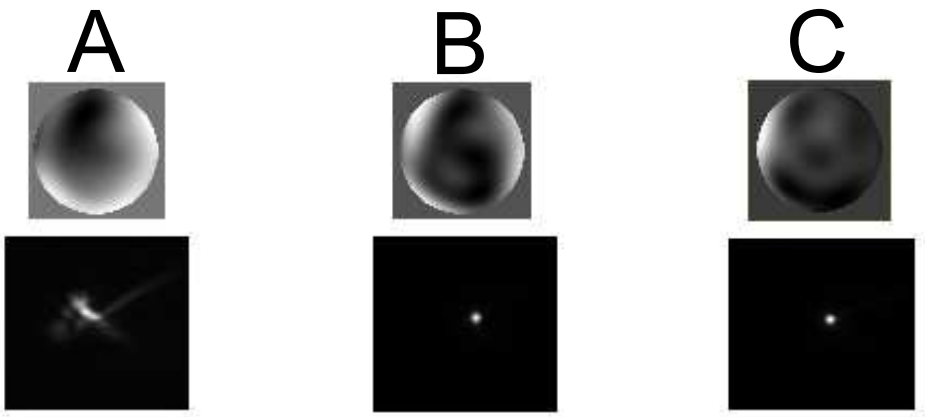

Figure 5.4: Each column contains two images. The top image is the phase wavefront and the bottom is the PSF of a bead. Column **(a)** represents the image of a bead when the mirror's actuators are all set to 0. After only one cycle **(b)** displays the correction and **c** is after two cycles. The resultant PSF shows clear improvement.

The iterative Gerchberg-Saxton (GS) algorithm uses the intensity of the wave field measured on both the image and diffraction plane [64]. Starting with an initial guess for the phase, the complex field is determined by using the two-dimensional Fourier transform and its inverse to iterate back and forth between the planes until it converges. At each iteration the amplitude of the image plane is corrected using the measured data. The GS procedure is diagrammed in Figure 5.5 [65].

This in itself, however, is an issue. The GS algorithm is susceptible to stagnation in which it may plateau or converge to local minima. In an effort to avoid this problem a new formula was devised [66]. It attempts to decrease the relative entropy criterion, known as the Kullback-Leibler (KL) divergence. Reducing the KL divergence can achieve a minimum value of zero when the data and model match perfectly.

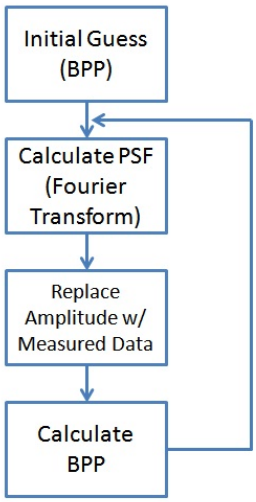

Figure 5.5: Simple representation of the iterative calculation using the Deming algorithm.

5.2.2 Applying Astigmatism

Using Equation 5.2, actuator commands can be calculated (a combination of Z_2^{-2} and Z_2^2) to create an astigmatic wavefront. The asymmetry of the wavefront (relative width along an orthogonal axis) can then be calculated at 10 nm z-intervals from a stack of images. Figure 5.6 demonstrates the change in the PSF as it progresses through the stack. Depth can be calculated from the asymmetry for an image of beads on the coverslip as shown in Figure 5.7.

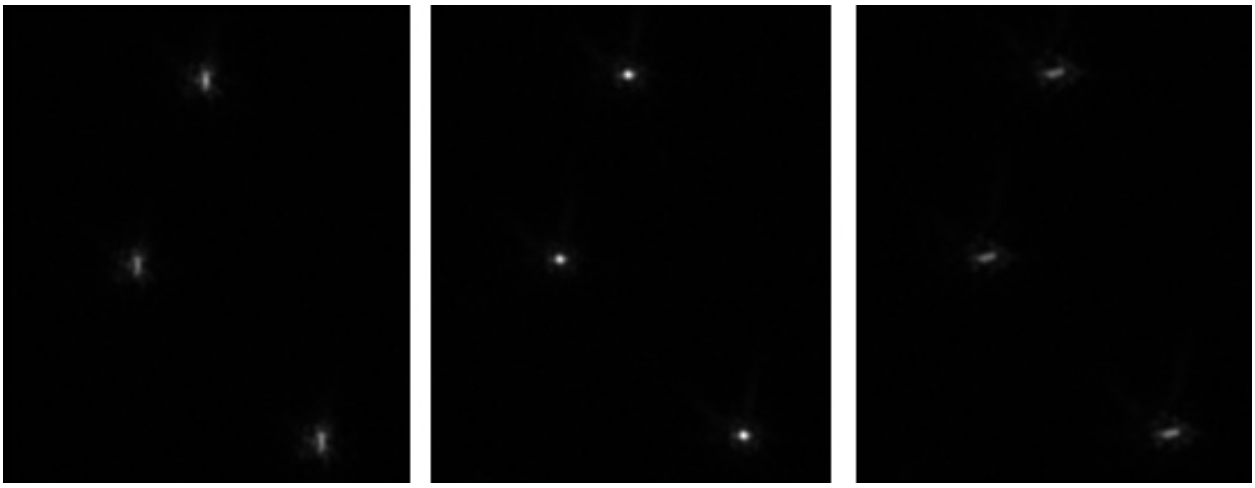

Figure 5.6: **(Left)** Beads found under the focus plane, z<0. **(Center)** Beads without astigmatism, or rather at z=0. **(Right)** Beads above the focus plane, z>0.

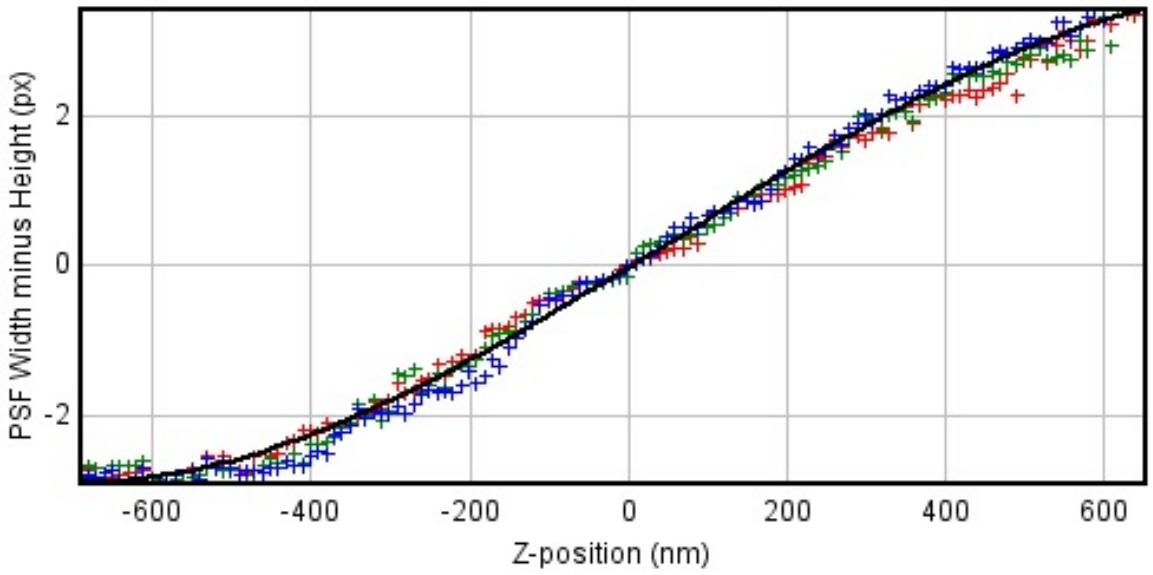

Figure 5.7: Fitting a curve to the three beads found in the previous figure. This regression may then be applied to other areas to create 3D structures.

Chapter 6

Experimental System

6.1 Optical Setup

An Olympus IX71 microscope with a PlanApo N 60x oil immersion objective is the first stage of the imaging system. The entire arrangement of the system can be seen in Figure 6.1. D1 and D2 are dichroic mirrors custom made by Omega Optical (495DCLP and 555DCLP respectively). Dichroics transmit some bands of wavelengths while reflecting other. D1, which reflects 500 nm and shorter wavelengths and transmits wavelengths greater than 500 nm, reflects the 488 nm Spectra-Physics Cyan excitation laser so it may travel through the objective and illuminate the sample. D2 has nearly zero transmittance between 510 nm and 540 nm, reflecting the emission wavelength into the camera after passing through D1.

As light is emitted from the sample, it is first collimated by the objective, and then re-imaged by the tube lens. The image plane is 102 mm off the side port of the microscope. Lenses L1 (Opto Sigma 026-1253) and L2 (Opto Sigma 026-1253) both have focal lengths of 350 mm. L1 re-collimates (lenses 1-5 are achromatic) the emission light again creating an image of the back pupil plane at the position of the Mirao 52-e deformable mirror. L2 creates an image plane prior to L3, which has a focal length of 100 mm. L3 (Opto Sigma 026-1170) again collimates the light.

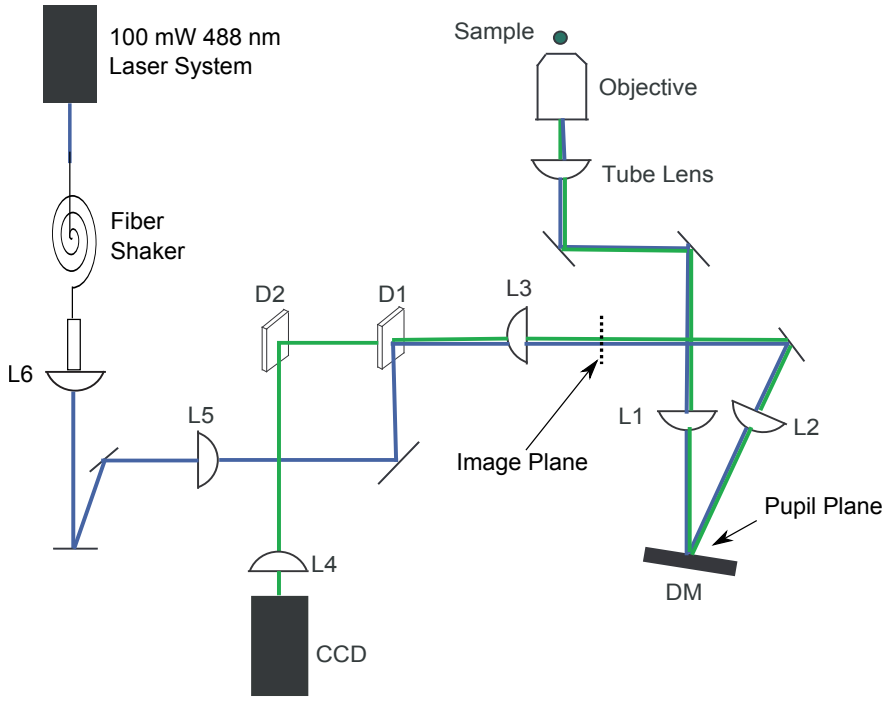

Figure 6.1: Optical setup with the blue beam being the excitation pathway and green the emission.

The final lens before the Andor EMCCD camera is L4 (Opto Sigma 026-1139). Its focal length is 300 mm and creates the recorded image plane at the CCD. The total magnification of the system results in an effective pixel size of 90 nm in the sample plane.

The excitation light from the 488 nm laser is coupled into a multimode fiber (100 μm core). A custom built fiber shaker is used to scramble the light uniformly into all the fiber modes. The light exiting the fiber is then collimated with L6 (F2405MA). L6 is an aspheric lens with a focal length of 8 mm, which is factory aligned to be one wavelength-adjusted focal length away from the fiber optic cable supplying the light. It acts to collimate the light to a narrower beam, giving us a higher intensity over a smaller area (918 μm^2). L5 (Opto Sigma 026-1250), focal length of 300 mm, creates a pupil plane just before D1.

6.1.1 Components

I. 4 x 6 8” thick optical table

II. Olympus IX71 Inverted Microscope with oil objective and DIC optics

III. Prior Proscan motorized xy stage with 200 micron travel piezo z-stage

IV. Spectra-Physics 100 mW 488 nm Cyan Laser System

V. Andor 512x512 pixel Ixon EMCCD Camera

VI. Imagine-Eye Mirao 52E Deformable Mirror

VII. Thorlabs Lenslet Array (150 micron pitch, 6.7 mm focal length) for

VIII. Wavefront sensing

IX. Photometrics Coolsnap HQ2 CCD Camera

6.2 Sample Preparation

6.2.1 Fluorescent Beads and QDs

Sparse samples of fluorescent beads and quantum dots on coverslips are imaged. The beads we use are yellow-green FluoSpheres (Invitrogen F8811), which are carboxylate modified microspheres with a 0.2 μm diameter. The QDs are Qdot 545ITK organic QDs (Invitrogen Q21791MP) that come in a 1 μM concentration. Each are mounted in the same manner. To start, the beads are diluted to a 1% solution and the QDs are diluted to 1:1000. These samples are then placed on a coverslip and allowed to air dry at room temperature. Once the sample is dry 10 μL of mounting solution is applied to the slide. The coverslip is then place onto the mounting solution and sealed using nail polish. If a QD blueing experiment is being performed, the mounting solution will have oxygen readily available, either PBS or H_2O. Otherwise, glycerol is used.

6.2.2 Zebrafish

Muscle fiber samples, found in Sections 6.2.2 to 6.2.4, are supplied by Elizabeth L. Brainerd's lab at Brown University. Their research specializes in the use of new microscopy techniques to gain knowledge of functional morphology and biomechanics of various species. STORM allows them to see far past the conventional resolution limits of confocal microscopy, and examine the mechanical function of muscle fibers.

Zebrafish muscle fibers are first fixed in Carnoy's solution for 4 hours at room temperature or overnight in the refrigerator. Then it is rehydrated through an ethanol series to DI. The sample is diluted with Proteinase K for 20 minutes and washed with phosphate buffered saline Triton-X100 (PBT) three times, 20 minutes each. The fibers are set in a solution of PBT/2% bovine serum albumin (BSA)/5% normal goat serum (NGS) for 30 minutes. Then washed with a primary antibody (5 μg/mL) for 4 hours at room temperature or overnight in the refrigerator. Again the muscle fibers are washed with PBT for 15 minutes, 5 times and then set in PBT/2% BSA/5% NGS for 30 minutes. In the final steps, the secondary antibody (1:100 dilution) is allowed to bind for 4 hours at room temperature or overnight in the refrigerator. The sample is washed with PBT and cleared with 50% glycerol and mounted on a coverslip in PBS.

6.2.3 Frog Sartorius

Frog sartorius muscle fibers are first placed in a 50% glycerin solution for 24 hours at -20° C. They are then washed in PBS for 5 minutes, blocked in a PBT/2% BSA/5% NGS solution for 20 minutes, and incubated with the primary antibody for 30 minutes. The process is repeated, first with a wash in PBT for 5 minutes and then another incubation, this time with the secondary antibody for 30 minutes. After a final wash in PBS for 5 minutes the sample is mounted on a coverslip in Fluorogel (Electron Microscopy Sciences 17985-10).

6.2.4 Rabbit Psoas

Glycerinated rabbit psoas muscle fibers are purchased from Carolina Biological. These are washed in PBS for 5 minutes and then blocked in PBT/2% BSA/5% NGS for 20 minutes. Samples are incubated with the primary antibody for 30 minutes, rinsed with PBT for 5 minutes, and then incubated with the secondary antibody for 30 minutes. A final wash with PBS for 5 minutes is performed and the specimen is then mounted on a coverslip in PBS.

6.2.5 *Toxoplasma gondii*

Samples are prepared by Boris Striepen's lab at the University of Georgia. Their research in cell and molecular biology revolves around protozoan parasites which are responsible for diseases such as malaria, opportunistic infections associated with AIDS, and fetal/childhood diseases. Because some parasites actually harbor remnant chloroplast organelles (apicoplasts), it becomes necessary to explore new drug delivery techniques associated with herbicides. Super resolution microscopy helps to better understand and dissect the apicoplast.

Confluent human foreskin fibroblasts grown on a glass coverslip were infected with 10^5 *Toxoplasma gondii* tachyzoites and incubated at 37°C. 24 hours after infection, coverslips were fixed with 4% formaldehyde for 20 minutes at room temperature, blocked with 3% Bovine serum albumin in phosphate buffered saline (PBS) for 20 minuntes, permeabilized with 0.2% triton X-100 in blocking solution for 20 minutes, and incubated with primary antibody (i.e. anti-tubulin or anti-IMC1) in permeabilization solution for 1 hour. Following 5 washes with PBS, coverslips were incubated with a goat anti-mouse Alexa 488 coupled secondary antibody for 1 hour and diluted in blocking solution. After another 5 washes with PBS, coverslips were mounted onto a glass slide using Fluoro Gel (glycerol based hardening mounting media from Electron Miscoscopy Sciences).

6.3 Detection and Image Building

Slides are mounted on the microscope and illuminated with a 488 nm cyan laser. An initial z-stack is taken at low intensity to give a general idea of the structure prior to bleaching. Afterward, the laser's amplitude is increased to the point of forcing Alexa 488 into the triplet state. At this point, the blinking of individual fluorohpores will be visible on the camera. Electron multiplying (EM) gain of the CCD is set such that no point is saturated (i.e. causing the input signal to max out the detector, losing information), in recent tests this value is typically 240, and then data collection begins. Image sets range from 10-50k images based on signal strength at the end of each session.

Custom software written in the Python programming language is used to control the microscope and acquire images. Priithon, a derivative of Python, is used to control the entire imaging apparatus. All control and data collection will be done via automated procedures without user interaction. Photon counts can be calculated from the CCD image data using the simple formula,

$$p = \frac{(ADC - b) * S}{G}. \tag{6.1}$$

Where p is the number of photons, ADC is the CCD value for a given pixel, b is the base level, S is the CCD sensitivity and G is the EM gain for the CCD. With an image taken at a 240 EM gain setting, the actual EM gain can be found using the graph in Figure 6.2. G is thus set at 700. With EM gain at 3 MHz the base level is 984 (noise is also amplified). The CCD sensitivity in EM gain mode is 23 electrons per ADC count. As an example, if a pixel has an intensity value of 5000 at 240 EM gain, then its corresponding photon count is $(5000 - 984) * \frac{23}{700} = 131$ photons.

After calculating an appropriate signal-to-noise ratio (SNR), QuickPALM [67] and RapidSTORM [68] analyze the raw data localize the emitting fluorophores. QuickPALM and RapidSTORM are freely available software programs for analyzing raw STORM images and creating the final high resolution image. Their respective graphical user interfaces are found in Figure 6.3. As stated, these two programs will be compared in their ability to reconstruct STORM images.

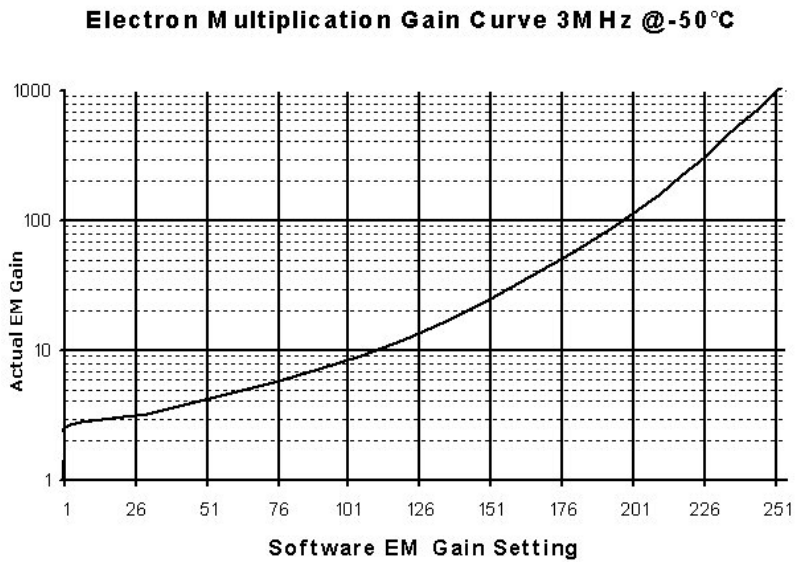

Figure 6.2: Graph relating software setting to actual gain found in the Andor EMCCD.

QuickPALM, an ImageJ plugin, has a less robust algorithm for finding PSFs, but supports virtual stacks enabling ImageJ to open files larger than the 1.5GB memory limit imposed on 32-bit systems. RapidSTORM is a stand-alone program, thus removing all of the filters and image analysis available in ImageJ.

After a set of images is opened, the location of interest on the screen, which is typically smaller than the entire field of view, is selected and cropped from the image to reduce computation time. Using data from the original image, an estimate of the SNR is determined by the user. This along with the image plane pixel size, size of the PSF, and any extra features that may be restricted (e.g. minimum symmetry in x and y, local thresholds, iterations per frame) are entered into the necessary data fields.

QuickPALM then analyzes each image finding fluorophore emission events while discarding any noise or odd features. Seemingly the program worked quite well, but it was very reliant on user inputs to find as many valid fluorescence emission events as possible. While it did detect blinking

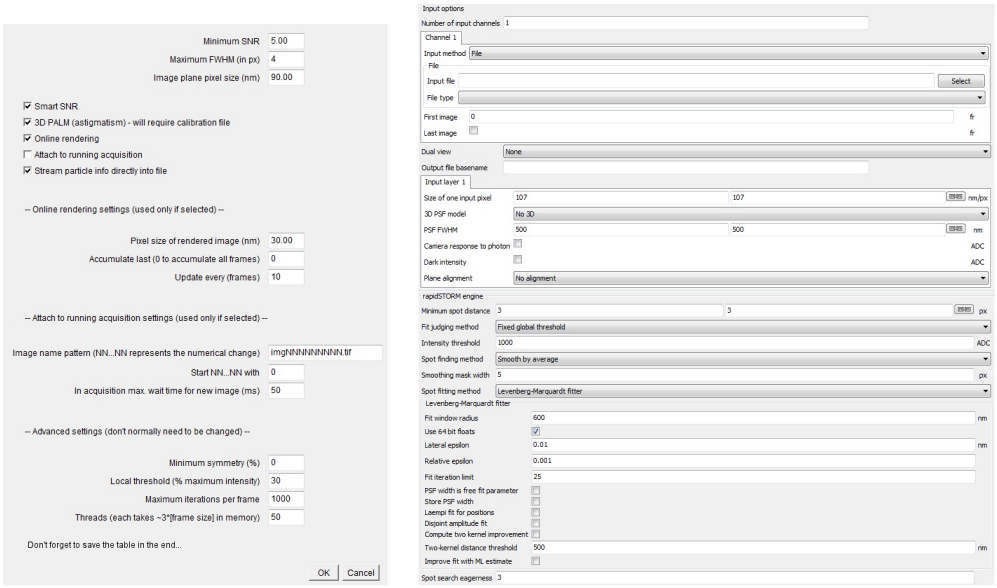

(a) QuickPALM (b) RapidSTORM

Figure 6.3: Image **(a)** represents the graphical user interface for QuickPALM and **(b)** for RapidSTORM.

particles, it also missed a large number due to varying SNRs. This is mostly due to the inability to set a SNR for a given fit window. QuickPALM calculates the SNR based on the mean intensity of the image, which causes high SNR points with low intensity to still not be recorded correctly.

RapidSTORM takes a different approach to registering valid particles. First, noise reduction is performed by smoothing each frame. This is done through either an average mask, median mask, Gaussian kernel mask, a morphological erosion or morphological fillhole transformation followed by erosion. Due to general speed and accuracy proven in recent research [68] we will be using the average mask. Rectangular masks, with window size based on calculated ideal PSFs, were used for the average filter. Local maxima are found by using the non-maximum suppression algorithm [69] by the same window size as the averaging mask. A list of local candidates is then identified and sorted by intensity. Candidates are fitted in descending intensity order. This process continues

Table 6.1: Noise reduction algorithms compared at different amplitude thresholds [68].

Specimen	Ampl. thresh.	Average		Gaussian		Erosion		Fillhole		Median	
		Rc.	Pr.	Rc.	Pr.	Rc.	Pr.	Rc.	Pr.	Rc.	Pr.
Spot finding time for a single image in ms		0.05		0.08		0.22		0.36		0.51	
Specimen 1 (small spots, low noise)	125	71%	93%	74%	20%	73%	98%	73%	99%	73%	98%
	156	69%	96%	70%	38%	70%	99%	70%	99%	70%	99%
	187	63%	96%	65%	52%	64%	99%	64%	99%	64%	99%
	250	58%	98%	58%	76%	59%	99%	59%	99%	59%	99%
Specimen 2 (large spots, high noise)	125	62%	71%	69%	12%	57%	61%	56%	77%	59%	79%
	156	61%	83%	67%	36%	57%	79%	56%	89%	58%	90%
	187	59%	91%	65%	35%	55%	93%	54%	95%	57%	95%
	250	57%	98%	58%	93%	54%	99%	54%	99%	55%	99%

Table 6.2: Comparison of the spot fitting and judging stage with different approaches [68].

Quantity	Recall	Fixed	Free
False positives	80%	23.34 ± 0.36	116.12 ± 9.27
per 10^4 fits	60%	1.62 ± 0.09	7.29 ± 0.44
to noise	40%	0.32 ± 0.03	0.70 ± 0.06

until a number of fit attempts fail (three by default). Successful attempts are localized on the final picture and a raster image with a 10 times greater resolution is displayed.

It becomes increasingly important with denser slides to determine the difference between a false and true positive. RapidSTORM demonstrates impressive speed and accuracy in this regard. Using the average mask filter, a spot is found every 0.05 ms. The Rc. columns found in Table 6.1 are the recall, or rather the percentage of present fluorophore emissions the software correctly found and localized. Pr. gives the precision, the overall localizations that belong to actually present fluorophores with the rest being false positives. Besides selecting the type of noise reduction, users have the option of entering in a fixed covariance matrix or free parameters to judge and fit the found points of interest. Interestingly enough, the fixed matrix had fewer false positives than the

free parameters, as seen in Table 6.2. It is unexpected that the fixed matrix performs better as there are fewer degrees of freedom available for fitting. However, that effect is diminished by higher noise tolerance which causes the nose distortions to cancel out in the covariance matrix.

Despite it's robust algorithm, there is only one crucial user input for RapidSTORM so that it may detect points correctly. This is the PSF of the optical system. Measuring the PSF requires an image of a bead using conventional fluorescence methods. Values are recorded and then fit to a Gaussian to create an estimate of the FWHM. X and Y pixels values for the FWHM of a bead are 3.202 and 3.036 pixels respectively, Figures 6.4 and 6.5. 90 nm corresponds to the length of one pixel. Therefore our system's PSF for diffraction limited objects with a 488 nm laser is $\sim$270 nm.

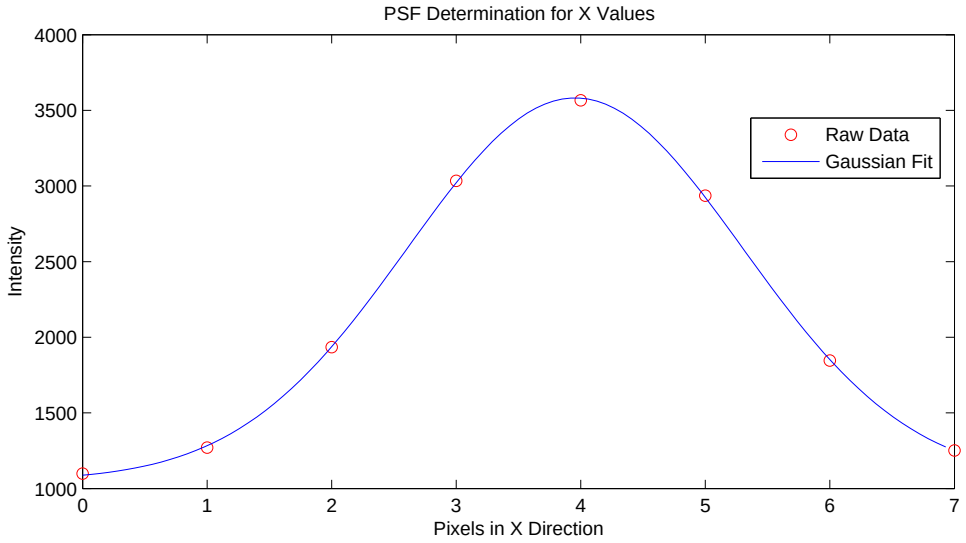

Figure 6.4: Gaussian fit to the image of a 200 nm fluorescent bead along the x axis. The fit provides an experimental measurement of the PSF width for use in the STORM analysis.

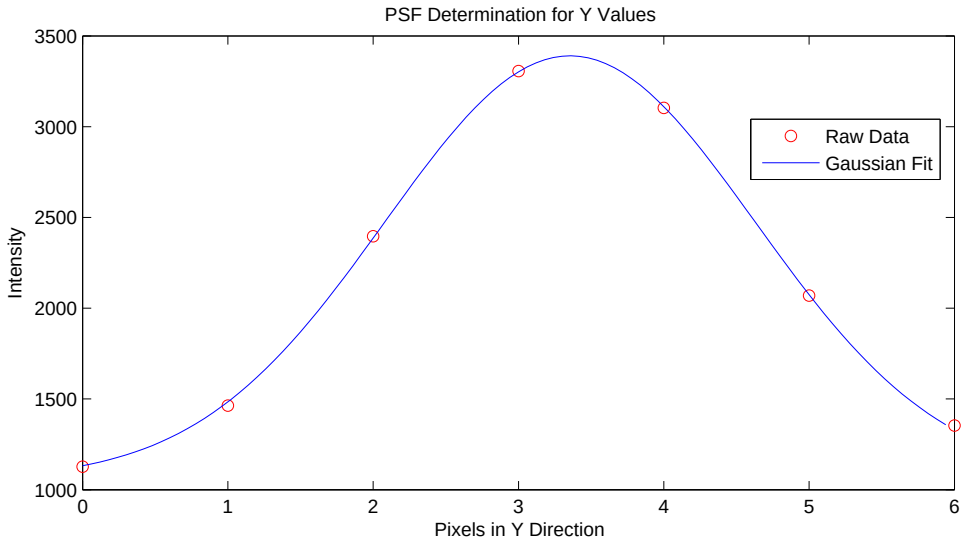

Figure 6.5: Gaussian fit to the image of a 200 nm fluorescent bead along the *y* axis. The fit provides an experimental measurement of the PSF width for use in the STORM analysis.

Chapter 7

Imaging

7.1 Imaging of Quantum Dots

QDs are dried onto a coverslip and then mounted in water to begin the blueing process discussed in Section 4.3. The images taken are then analyzed and the resulting data is seen in Figure 7.1. This sample is extremely sparse allowing for an easy STORM reconstruction.

7.2 Muscle Fibers

In this section, we discuss the STORM imaging of muscle fibers supplied to us from Dr. Brainerd's lab. The Brainerd lab is interested in Titin, a passive protein thought to be the scaffolding of a sarcomere, and its role in muscle contraction. STORM offers obvious resolution gains which are attractive to any biologist pursuing knowledge of a protein's structure. These fibers were labeled for Myosin to test the sarcomere length.

These are the first STORM images captured by our system in 2011 using zebrafish, Figure 7.2. A major limitation when viewing the muscle fibers sent to us is the depth. Most of these samples were hundreds of microns thick. Each sample has a high background intensity which interferes

with the localizations to the point that resolution is lost due to out of focus light. We demonstrate that blinking is perfectly capable within such thick samples. Even without any adaptive optics to correct the PSF, we are able to acquire some resolution gain. However, these images highlight the need to pair AO with STORM.

Reduction of the background came by sectioning thinner samples and using different samples. Figure 7.3 is frog sartorius muscle, which is a long muscle that covers the anterior surface of the thigh. It originates on the pubis and inserts on the tibiofibula to flex the thigh. Figure 7.4 is rabbit psoas muscle fibers. The psoas is striated muscle that rotates the hip joint and flexes the spine. Both of these samples are an improvement because they are long and straight and have a relatively small amount of connective tissue associated with them.

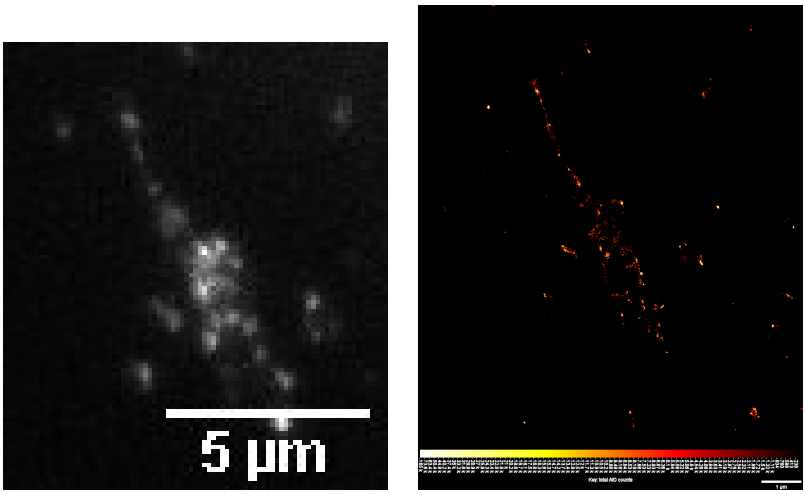

(a) Widefield Fluorescence (b) RapidSTORM Result

Figure 7.1: Image **(a)** is the conventional widefield image of QDs on a coverslip, **(b)** is the RapidSTORM reconstruction after recorded blinking events from blueing. The images are equivalent in size and the 1 μm scale bar, which is small due to downsampling, is found in the bottom right of the RapidSTORM image. This is the same for all comparison images in this paper.

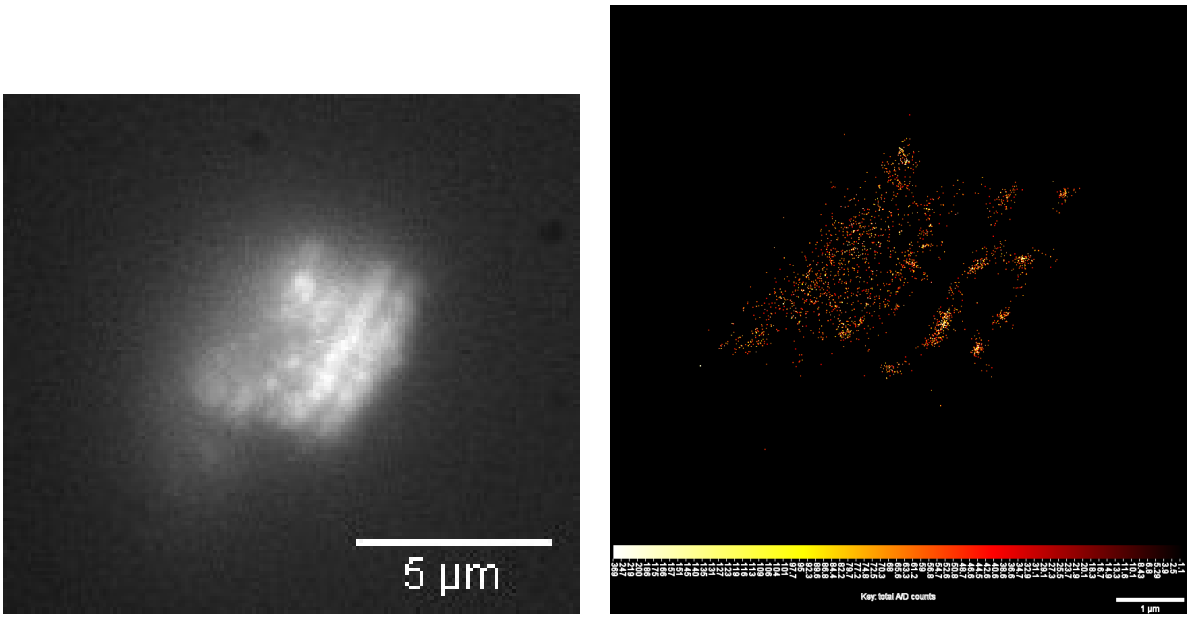

(a) Widefield Fluorescence (b) RapidSTORM Result

Figure 7.2: Image **(a)** is zebrafish muscle fibers, found in the tail, being imaged by widefield fluorescence, and **(b)** is the RapidSTORM reconstruction after STORM imaging.

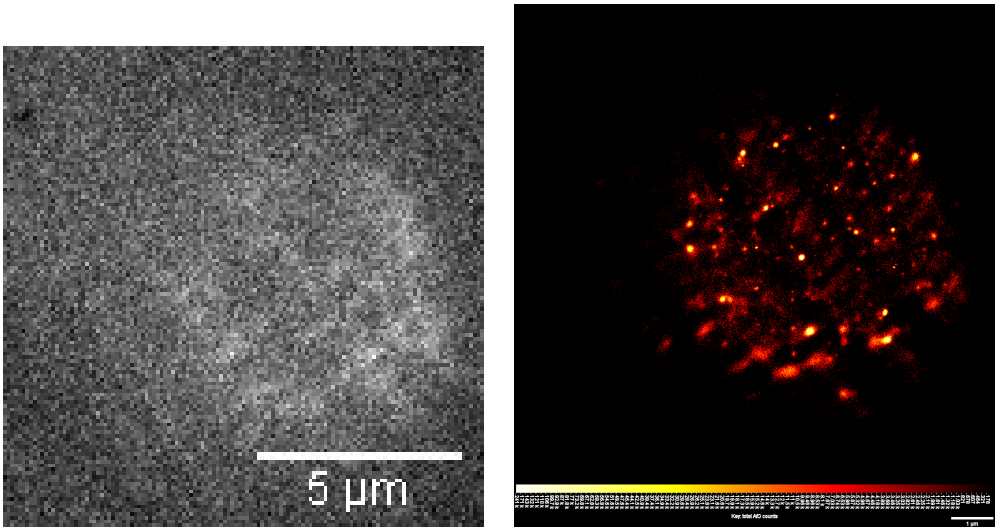

(a) Widefield Fluorescence (b) RapidSTORM Result

Figure 7.3: Image **(a)** is frog sartorius muscle fibers being imaged by widefield fluorescence, and **(b)** is the RapidSTORM reconstruction after STORM imaging.

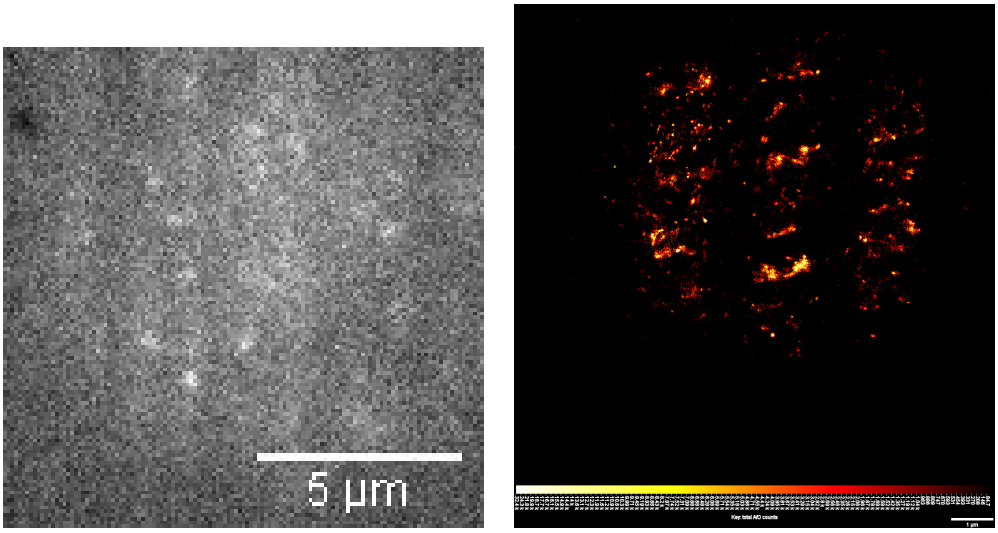

(a) Widefield Fluorescence (b) RapidSTORM Result

Figure 7.4: Image **(a)** is rabbit psoas muscle fibers being imaged by widefield fluorescence, and **(b)** is the RapidSTORM reconstruction after STORM imaging.

7.3 *Toxoplasma gondii*

We performed STORM imaging on microtubules in *Toxoplasma gondii* labeled with Alexa 488. Alexa Dyes have been used extensively in STORM [70]. The antibodies were specific to tubulin, which have a general width of 20 nm in this sample. Prior to STORM and eventual bleaching of the sample, a z-stack (Figure 7.5) is taken to have an idea of the beginning structure. Fifty-thousand pictures were taken and cropped so that analysis is only performed on the relevant section of the image, removing extraneous computing time.

Both RapidSTORM and QuickPALM are used to analyze the raw data. Their respective reconstructions may be seen in Figure 7.6. In the RapidSTORM reconstruction, the pixel size is 10 nm. QuickPALM's final pixel size is 20 nm. It can be plainly seen that the RapidSTORM reconstruction detects more points and thus attains a higher localization. Using RapidSTORM's image, a line

plot (Figure 7.7) is then used to find the intensity along the width of an apparent tubulin structure. Taking the FWHM of the plot, the reconstructed structure has an apparent width of 30 nm.

Figure 7.6 is an example of an image that has a portion of well resolved microtubules. However, the initial phase of this STORM system had many poorly resolved images. These original tests were mounted only in a PBS solution. More often than not a final image resembled Figure 7.8. In the last two years, more research has been done on the buffer and its affect on blinking. These results [42, 71] demonstrate that STORM with Alexa 488 works best in a 100 mM MEA buffer with pH 7.4-8.0. Figure 7.9 is the final image in this "blinking solution". The increase in SNR in the final image is a direct result of more blinking. Other concentrations of MEA were tested, but the higher the MEA the more damaging to the cell, and lower concentrations had little to no affect. Also MEA solutions have a relatively short shelf life and produce negative results if fresh buffer is not made. MEA is kept frozen when not in use, as storing it at room temperature would only preserve the solution for 24 hours.

The final method using Alexa 488 uses shorter wavelength light to re-excite the seemingly bleached fluorophores. Every 500 images 10 seconds of low power 405 nm LED light illuminates the sample. This extends the blinking lifetime of Alexa 488 and thus the localization accuracy. Figure 7.10 is the widefield and RapidSTORM detected localizations. Figure 7.11 is an overlay demonstrating the gain in resolution.

Blueing of QDs is facilitated by oxidation of the CdSe core. Images are taken with intervals ranging on the order of seconds. This process takes much longer than the blinking seen with Alexa 488. The buffer for this technique is 100% de-ionized water. As oxidation is the driving process behind blueing, the more available oxygen present, the faster the process will take place. Unfortunately, the labeling process for this parasite caused poor resolution in Figure 7.12.

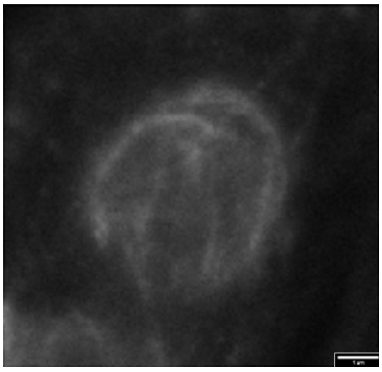

Figure 7.5: Conventional wide-field image taken before any bleaching or STORM data acquisition. Resolvable tubulin structures can only be seen on the edges of the cell wall. The scale bar represents 1 μm.

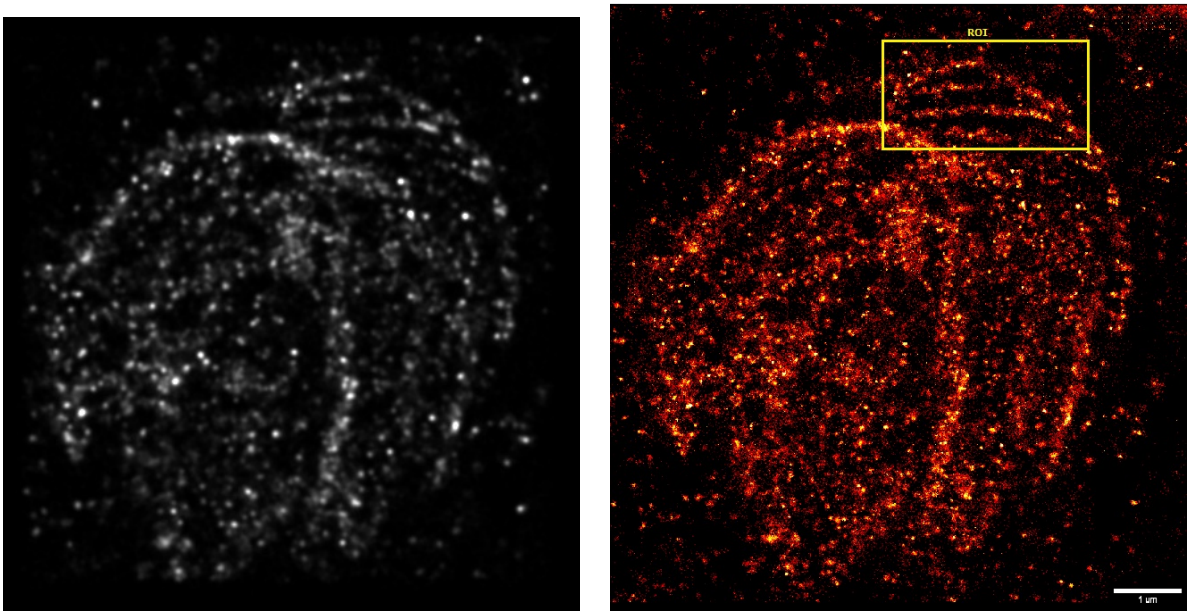

(a) QuickPALM Result

(b) RapidSTORM Result

Figure 7.6: Image **(a)** is the QuickPALM reconstruction of anti-tubulin and **(b)** is the RapidSTORM reconstruction with the same data.

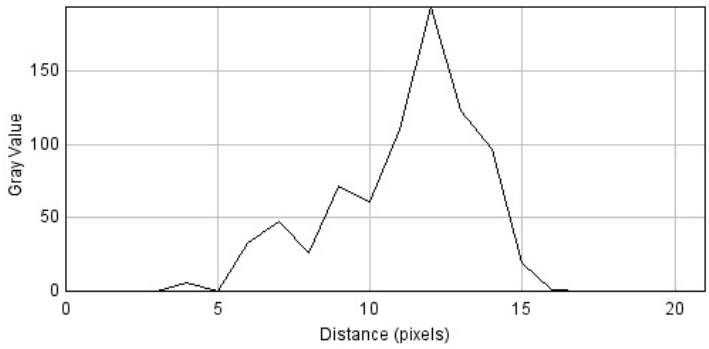

Figure 7.7: A line plot across the tubulin structure in the RapidSTORM reconstruction.

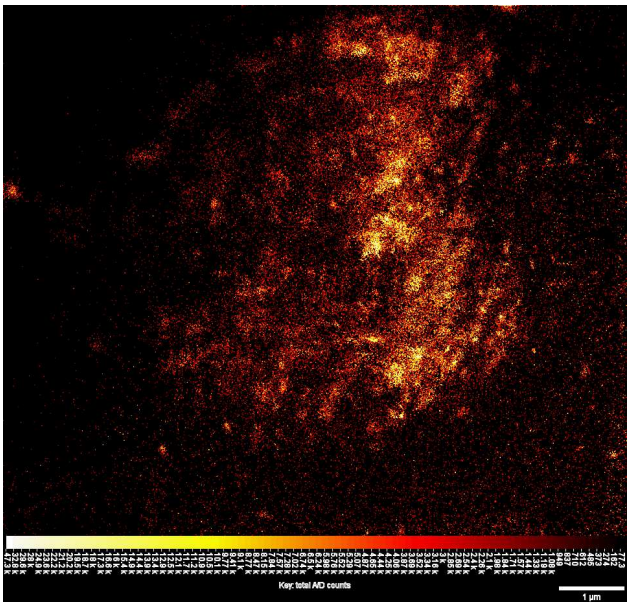

Figure 7.8: Poorly resolved STORM image, *Toxoplasma gondii* in PBS, typically seen during the early development stage of our optical system.

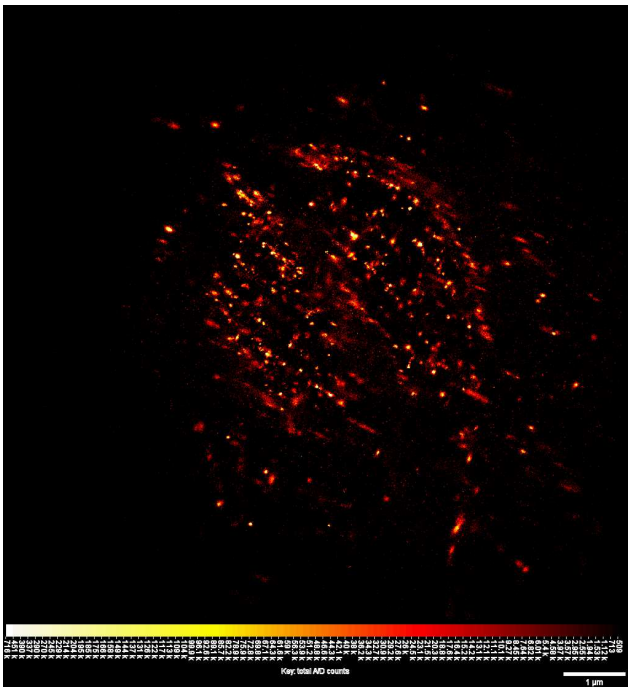

Figure 7.9: Well resolved image of *Toxoplasma gondii* with a 100 mM concentration of MEA in PBS.

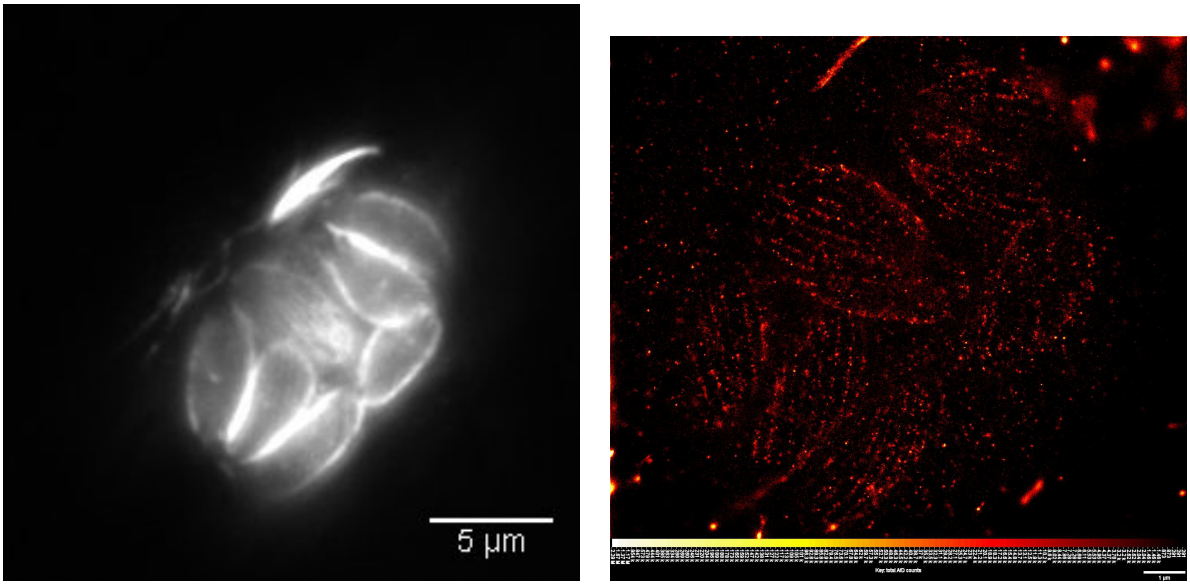

(a) Widefield Fluorescence

(b) RapidSTORM Result

Figure 7.10: Image **(a)** Widefield fluorescent image of *Toxoplasma gondii* prior to STORM. Microtubules are not completely resolved. **(b)** STORM with shorter wavelength, 405 nm, laser pulses. These pulses act to increase the blinking lifetime of the fluorophores allowing for greater precision.

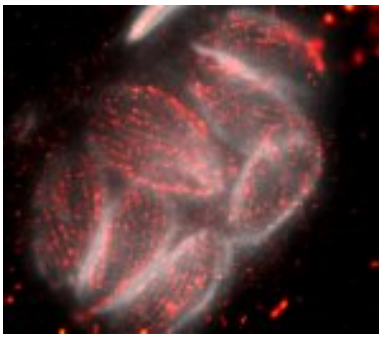

Figure 7.11: STORM localizations superimposed on top of Figure 7.10.

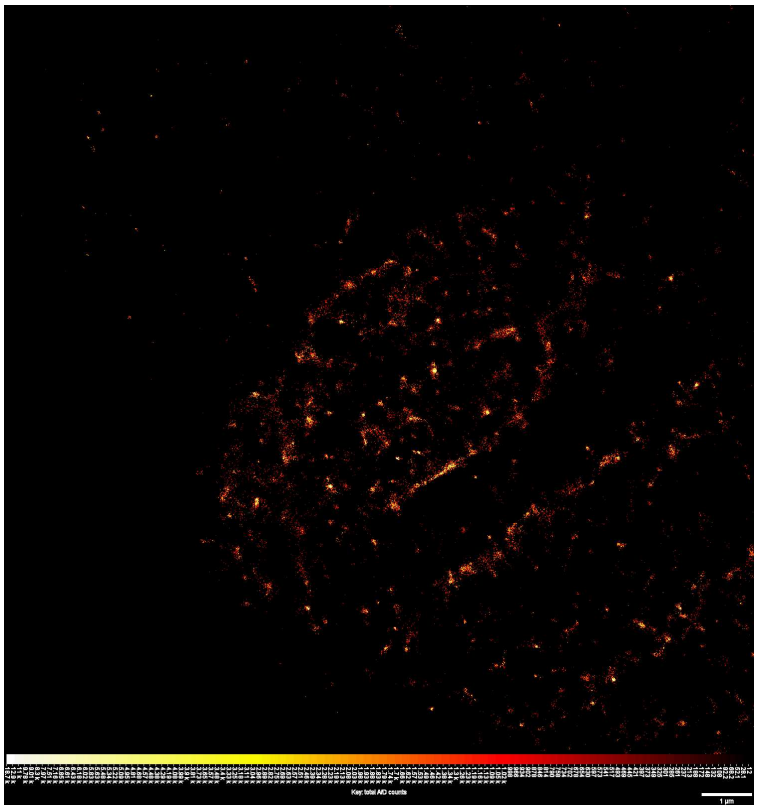

Figure 7.12: *Toxoplasma gondii* labeled with CdSe quantum dots.

7.4 3D *Toxoplasma gondii* Image

The astigmatic PSF technique is used to acquire 3D information, which is described in Section 2.2.2. However, our lab is using a deformable mirror to create astigmatism, Section 5.2.2, which is an unconventional approach to applying astigmatism. The sample preparation for 3D images is identical, and the mounting buffer is only PBS. Re-excitation by a shorter wavelength light source is used instead of MEA in this technique. RapidSTORM calculates the calibration curves and fits spots based on their asymmetry, using an interpolated 3D PSF data set. The final image is seen in Figure 7.13.

In order for RapidSTORM to localize these astigmatic PSFs, it requires a much larger fit window. This is due to the tails of the PSF. They must be included in order to best fit the asymmetry and correlate it with depth. These larger fit windows, however, seem to cause issues with tracking positive emitters. The apparent loss in resolution is partly attributed to this.

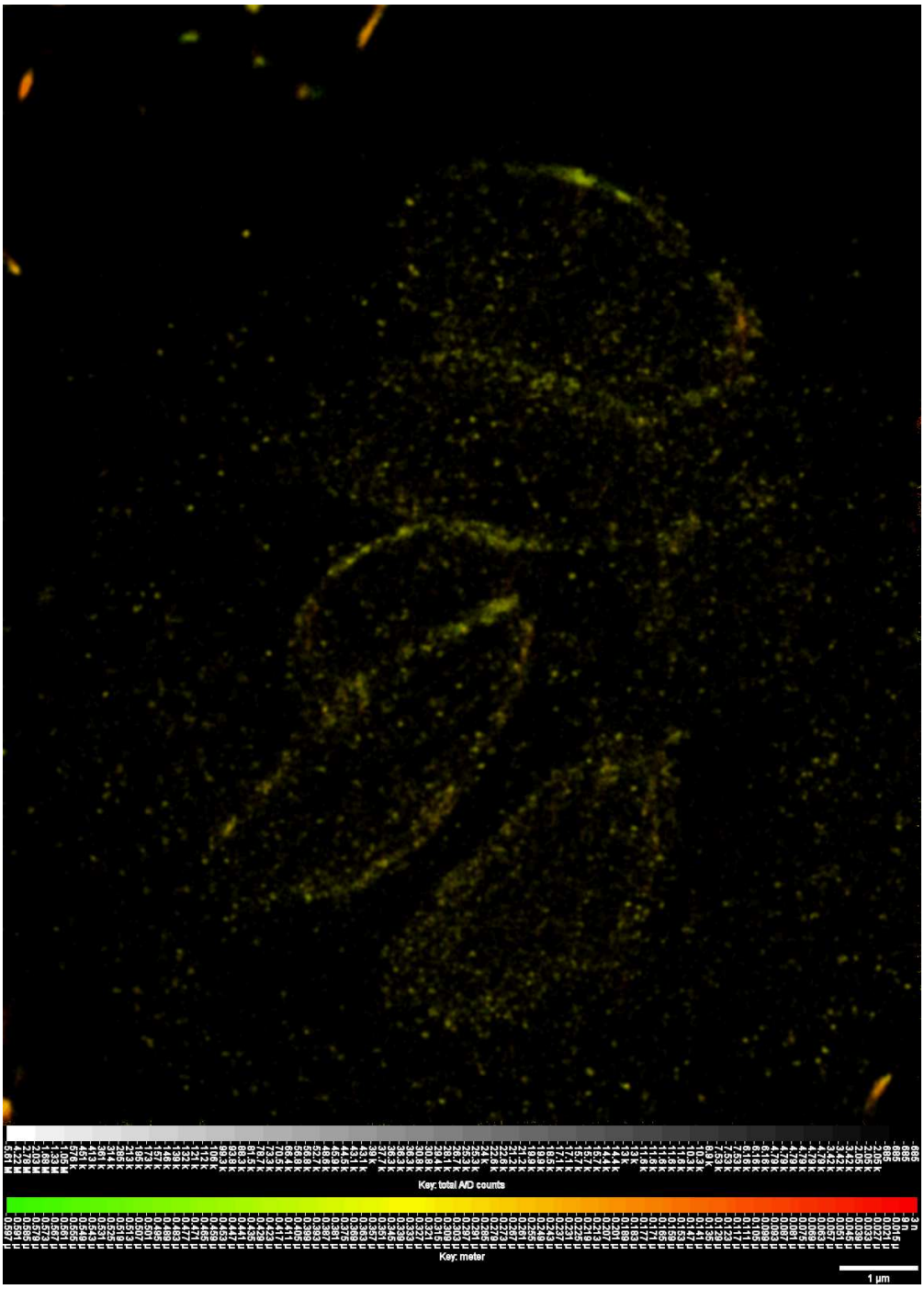

Figure 7.13: An example of taking a 3DSTORM image of *Toxoplasma gondii* with Alexa 488 as the molecular marker. Re-excitation is used to prolong lifetime and extend the blinking of the dye. Change in color depicts a change in depth.

Chapter 8

Photon Statistics

Equation 2.4 establishes the relationship between localization precision and photons, more photons detected results in higher precision. In this chapter we will compare histograms, describing photon statistics, of images using STORM to resolve *Toxoplasma gondii*. As exposure rate is the time the camera collects photons from an excited source, it thus varies linearly with the number of photons. If the camera exposure is longer, the photon counts will be higher. The same can be said for excitation laser intensities. There is a direct relationship between laser power and photon count. In order for these images to be compared, the exposure rate and laser intensity are taken into consideration. For all images, unless otherwise stated, the exposure rate is 20 ms. This is guaranteed by setting the Andor EMCCD to frame transfer mode. In this mode the minimum exposure rate is limited by the speed at which the CCD can read and empty the wells. Each image is 256 by 256 pixels, thus each has the exact same exposure rate. The laser power does vary slightly, but it is always within 25±3 mW. The resulting spot has a laser intensity of 915 $^{W}/_{cm^2}$, previous literature uses $\sim$1000 $^{W}/_{cm^2}$. Another factor to take into account for photon counts is bleaching and the eventual dimming of emitters. In an attempt to negate this effect, only the first 1000 localizations (15-30 per frame) are used in the following histograms, Figures 8.1 to 8.3. Otherwise the counts would be skewed toward lower intensity values.

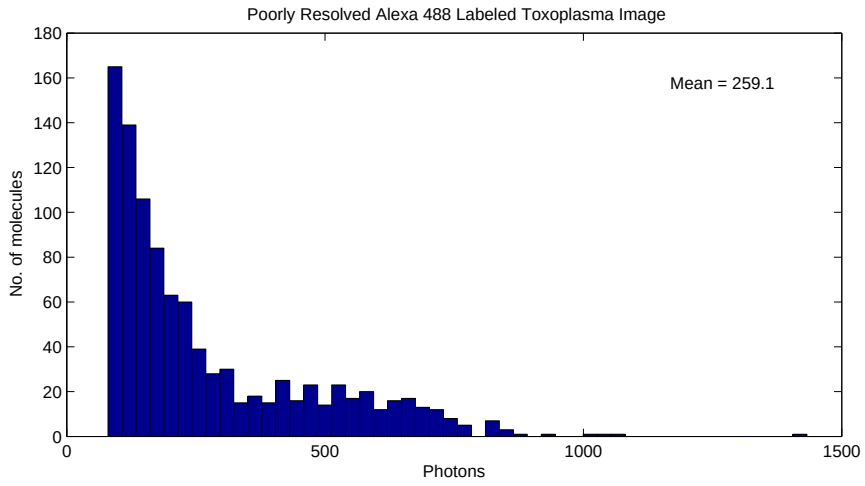

Figure 8.1: Photon statistics for a poorly resolved image, based on Figure 7.8.

To reaffirm that quantum dots emit more photons, an experimental sample is placed on a coverslip in an aqueous buffer rich in oxygen. This sample actually produces so many photons that no EM gain is required to amplify the signal. The signal from the CCD is converted to photons by Equation 6.1. Statistics are compared to the conventional dye used in dSTORM, Alexa 488. Figures 8.4 and 8.5 include the mean value for the measured data.

One concern for the blueing process is if the conventional photon relationships still apply. In other words, if photon counts still vary linearly with intensity and exposure rates. Figures 8.7 to 8.9 measure the photon statistics for different laser intensities. The mean values are found and fit linearly in Figure 8.10.

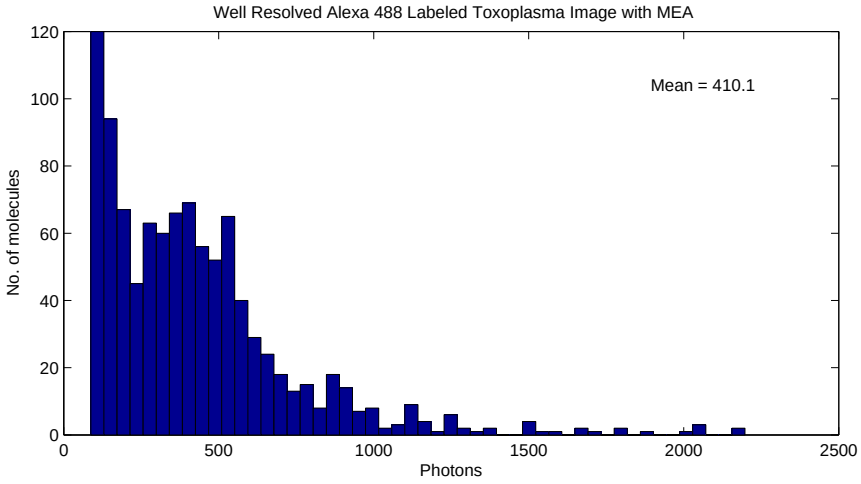

Figure 8.2: Photon statistics for a well resolved image with MEA, based on Figure 7.9.

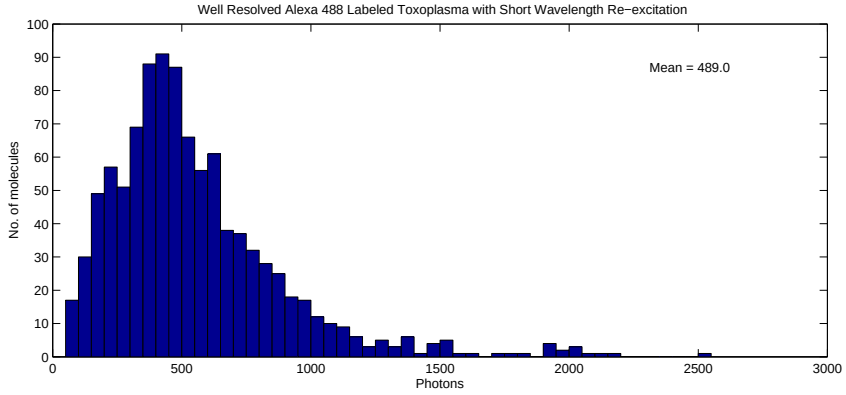

Figure 8.3: Photon statistics for a well resolved image using shorter wavelength re-excitation, based on Figure 7.10.

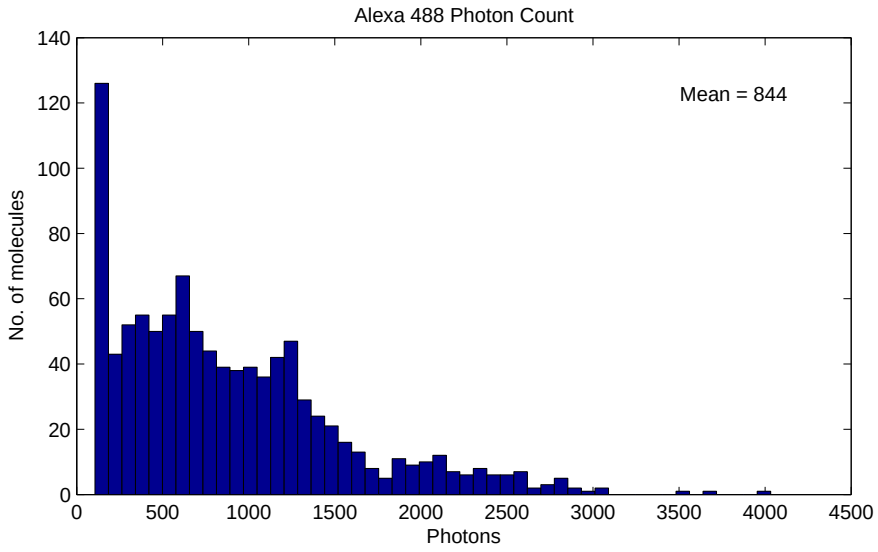

Figure 8.4: Alexa 488 photon statistics for a well resolved image.

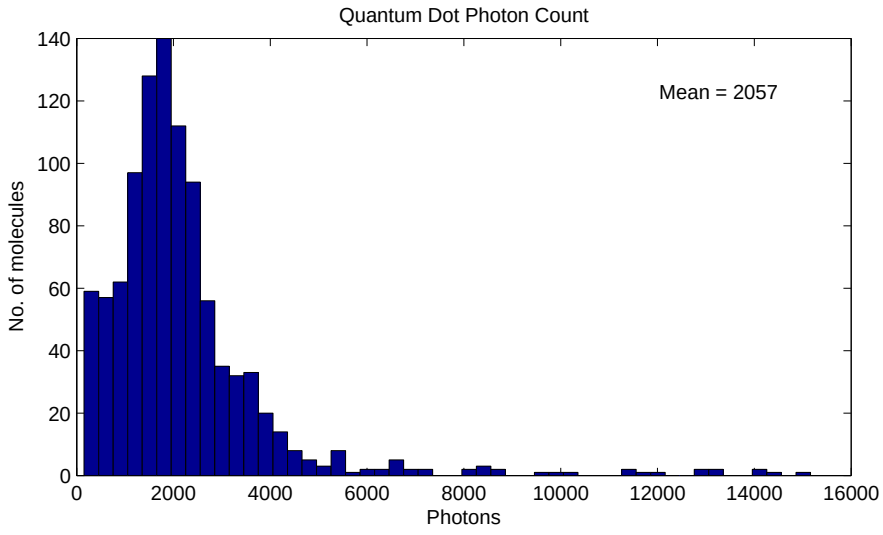

Figure 8.5: CdSe quantum dots on a coverslip.

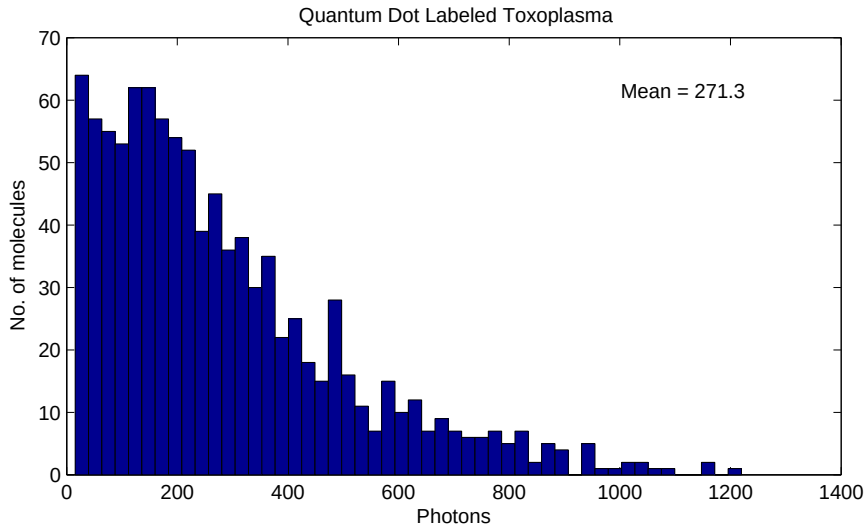

Figure 8.6: Photon statistics for QDs tagged to *Toxoplasma gondii*, Figure 7.12.

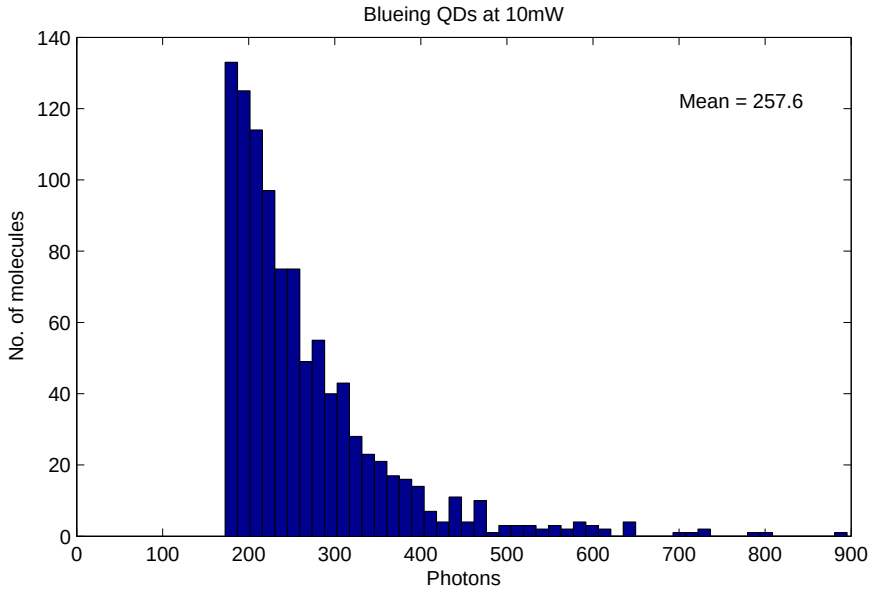

Figure 8.7: Testing photon counts for QDs using the blueing technique at 10 mW laser power.

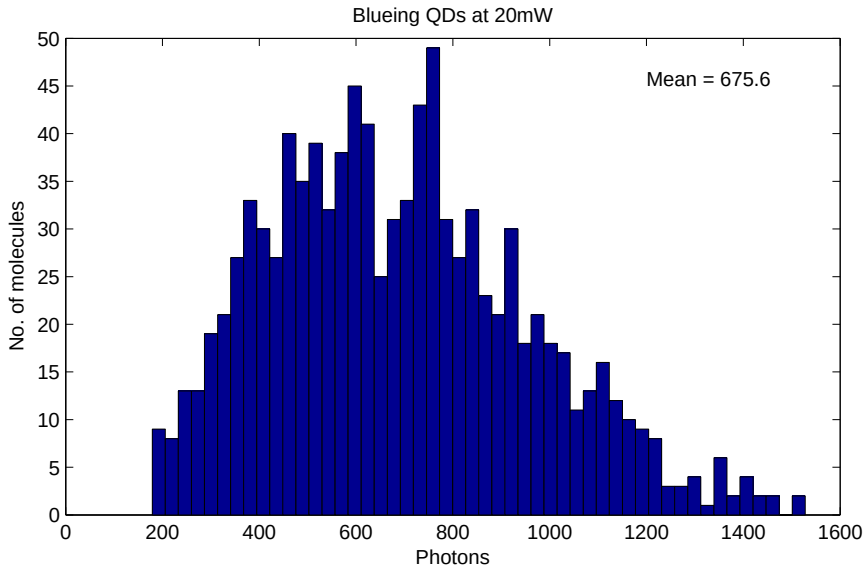

Figure 8.8: Testing photon counts for QDs using the blueing technique at 20 mW laser power.

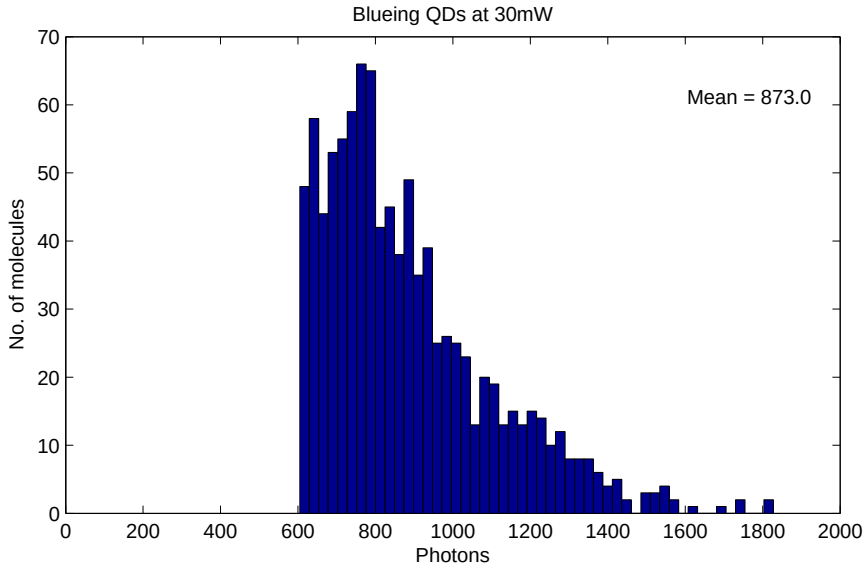

Figure 8.9: Testing photon counts for QDs using the blueing technique at 30 mW laser power.

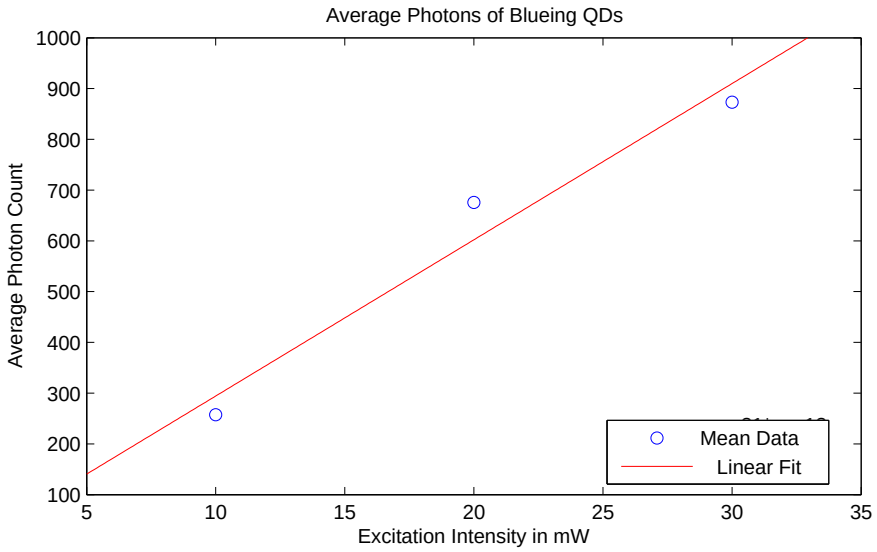

Figure 8.10: Plot displaying the linear relationship between intensity and photon counts even during blueing. This test simply demonstrates that blueing experiences the same relationship between intensity and photons as do normal fluorophores.

Chapter 9

Discussion

The purpose of this research project is to re-create STORM and then improve its viability in thick samples through the addition of adaptive optics and QDs. We were able to create a STORM system that reliably images well labeled samples with $\sim$30 nm resolution. The adaptive optics system corrects aberrations found in our optical setup to create a near perfect PSF, and also is used to induce measurable astigmatic aberrations on samples to create 3D images. QD's blueing process is examined and compared to conventional methods and then is used to localize an experimental setup. Each of these may be improved through various methods and need to be combined in future work.

We demonstrate STORM by imaging multiple muscle and *Toxoplasma gondii* samples labeled with Alexa 488 and achieve resolutions of 30 nm, revealing previously unresolvable tubulin structure. Each sample provides a set of challenges. The muscle is so densely labeled that we must bleach most of the background light out in an attempt to get a high enough SNR to see blinking. Likewise, a major drawback in using *Toxoplasma gondii* is that they must be grown in human fibroblasts. Fibroblasts, themselves, have a substantial amount of tubulin structure and are also stained with Alexa 488 anti-tubulin markers. This reduces the SNR of the desired structure. Over time, more specific antibodies (α-tubulin) were used in an attempt to lower background noise.

These markers paired with new buffers and excitation techniques led to a noticeable difference in image quality.

In order to draw conclusions in improvement we need to first prove our Alexa dye behaves correctly. Figure 8.4demonstrates that our photon values for Alexa 488 conform to prior literature [41]. Equation 2.2 states that there is a direct correlation with photon statistics and resolution. Our resulting histograms tell the same story. All images with photon counts less than 400 did not compile into a highly resolved image. Those higher show impressive resolution gains.

MEA accomplishes this by increasing the number of switching events and extending the time spent in the triplet state. Re-excitation increases the lifetime of a fluorophore by causing a conformational change, shifting the molecular marker out of a non-fluorescent state. The re-excitation method is easier to reproduce and does not require any manipulation of the sample. MEA, on the other hand, literally damages the cell the longer it is in contact, which causes samples to degrade over time.

Also, MEA can become unstable if not stored correctly or used in a short time period. Reported results using MEA [42, 71] show that a pH of 7.4-8.0 is ideal for blinking. Our buffer's pH is currently 10, measured with pH test strips. This may be causing a decrease in photon counts and therefore a lower resolution. Overall, re-excitation via shorter wavelength had the same advantages with a less complex mounting and imaging technique. Both the addition of MEA and use of the re-excitation laser lead to a gain in resolution by increasing photon counts.

We successfully corrected our system with adaptive optics and calibrated an astigmatic PSF in use with 3D imaging. However, 3DSTORM did not show as much resolution in the axial direction as expected. This is attributed to the same issue found with other *Toxoplasma gondii* images. The vast number of tubules that are labeled in 3D space cause for incorrect localizations. In other words, tubules in the fibroblast blink in the same space as those in the *Toxoplasma gondii*, causing the algorithm to mark true positives for points not found on the desired structure. Samples with

a higher specificity or reduced background labeling will cause an increases in resolution for both conventional STORM and 3DSTORM.

Quantum dots display the same characteristic exposure/intensity pattern as seen in conventional fluorophores. We also achieve a partially resolved image using blueing in *Toxoplasma gondii*, but no well resolved images were captured. There are currently issues with our labeling protocol for QDs and *Toxoplasma gondii*. To test the protocol, we need to replicate the labeling procedure used in the original blueing article. It is possible that *Toxoplasma gondii* is too small to allow the QDs to migrate into the necessary areas. We experienced a similar issue when we attempted labeling zebrafish with QDs.

The next step is extending this system so it may perform STORM on thick samples. STORM, being reliant on high SNR and therefore low background noise, does not perform well viewing through turbid media. Using the deformable mirror can correct for any phase changes the light may experience. In addition, applying astigmatism will allow for optical sectioning in these environments. Therefore more focus should be placed on improving the 3DSTORM methodology in our system.

Appendix A

First Appendix

A.1 SOFI Code in Python

```
def SOFI(img):
        orig = img.shape
        leng = orig[1]*orig[2]
        img = img.reshape(orig[0], leng)
        new = img.shape #Changes shape to a line of pixels
        sbuild1 = F.zeroArrF((orig[1]*orig[2]))
        for i in range(new[1]): #Iterates through each pixel
            a = ((img[:,i]-img[:,i].mean(0)))*((img[:,i-1]-img[:,i].mean(0)))
            sbuild1[i] = a.sum(0)
            print i,leng
            Y.refresh() #Calculates the fluctuation events
        sbuild1 = sbuild1.reshape(orig[1], orig[2])
        Y.view(sbuild1) #Produces final image
```

Bibliography

[1] David J. Stephens and Victoria J. Allan. Light microscopy techniques for live cell imaging. *Science*, 300(5616):82–86, 2003.

[2] Shimon Weiss. Shattering the diffraction limit of light: A revolution in fluorescence microscopy? *Proceedings of the National Academy of Sciences of the United States of America*, 97(16):8747–8749, 2000.

[3] Sripad Ram, E. Sally Ward, and Raimund J. Ober. Beyond rayleigh's criterion: A resolution measure with application to single-molecule microscopy. *Proceedings of the National Academy of Sciences of the United States of America*, 103(12):4457–4462, 2006.

[4] Derrick McNeill. http://www.ipodphysics.com/wave-resolution.php.

[5] David A. Agard and John W. Sedat. Three-dimensional architecture of a polytene nucleus. *Nature*, 302(5910):676–681, 1983.

[6] C Cremer and T Cremer. Considerations on a laser-scanning-microscope with high resolution and depth of field. *Microscopica acta*, 81:31–44, 2004.

[7] M. A. A. Neil, R. Juskaitis, and T. Wilson. Method of obtaining optical sectioning by using structured light in a conventional microscope. *Opt. Lett.*, 22(24):1905–1907, Dec 1997.

[8] M. G. L. Gustafsson. Surpassing the lateral resolution limit by a factor of two using structured illumination microscopy. *Journal of Microscopy*, 198(2):82–87, 2000.

[9] Stefan W. Hell and Jan Wichmann. Breaking the diffraction resolution limit by stimulated emission: stimulated-emission-depletion fluorescence microscopy. *Opt. Lett.*, 19(11):780–782, Jun 1994.

[10] Lothar Schermelleh, Rainer Heintzmann, and Heinrich Leonhardt. A guide to super-resolution fluorescence microscopy. *The Journal of Cell Biology*, 190(2):165–175, 2010.

[11] Michael J. Rust, Mark Bates, and Xiaowei Zhuang. Sub-diffraction-limit imaging by stochastic optical reconstruction microscopy (storm). *Nat Meth*, 3(10):793–796, 2006. 10.1038/nmeth929.

[12] Eric Betzig, George H. Patterson, Rachid Sougrat, O. Wolf Lindwasser, Scott Olenych, Juan S. Bonifacino, Michael W. Davidson, Jennifer Lippincott-Schwartz, and Harald F. Hess. Imaging intracellular fluorescent proteins at nanometer resolution. *Science*, 313(5793):1642–1645, 2006.

[13] Samuel T. Hess, Thanu P. K. Girirajan, and Michael D. Mason. Ultra-high resolution imaging by fluorescence photoactivation localization microscopy. *Biophysical journal*, 91(11):4258–4272, 2006.

[14] Russell E. Thompson, Daniel R. Larson, and Watt W. Webb. Precise nanometer localization analysis for individual fluorescent probes. *Biophysical journal*, 82(5):2775–2783, 2002.

[15] Norman Bobroff. Position measurement with a resolution and noise-limited instrument. *Review of Scientific Instruments*, 57(6):1152–1157, 1986.

[16] Ahmet Yildiz, Joseph N. Forkey, Sean A. McKinney, Taekjip Ha, Yale E. Goldman, and Paul R. Selvin. Myosin v walks hand-over-hand: Single fluorophore imaging with 1.5-nm localization. *Science*, 300(5628):2061–2065, 2003.

[17] M Bates, B Huang, and X Zhuang. Super-resolution microscopy by nanoscale localization of photo-switchable fluorescent probes. *Curr Opin Chem Biol*, 12:505 – 514, 2008.

[18] A Muller and J Grazul. Optimizing the environment for sub-0.2 nm scanning transmission electron microscopy. *Journal of Electron Microscopy*, 50(3):219–226, 2001.

[19] Samara L. Reck-Peterson, Nathan D. Derr, and Nico Stuurman. Imaging single molecules using total internal reflection fluorescence microscopy (tirfm). *Cold Spring Harbor Protocols*, 2010(3):pdb.top73, 2010.

[20] Warren R. Zipfel, Rebecca M. Williams, and Watt W. Webb. Nonlinear magic: multiphoton microscopy in the biosciences. *Nat Biotech*, pages 1369–1377, 2003.

[21] P Torok and T Wilson. Rigorous theory for axial resolution in confocal microscopes. *Optics Communications*, 137(13):127 – 135, 1997.

[22] Stefan W. Hell and Matthias Nagorni. 4pi confocal microscopy with alternate interference. *Opt. Lett.*, 23(20):1567–1569, Oct 1998.

[23] Mats G. L. Gustafsson, David A. Agard, and John W. Sedat. Sevenfold improvement of axial resolution in 3d wide-field microscopy using two objective lenses. pages 147–156, 1995.

[24] Bo Huang, Wenqin Wang, Mark Bates, and Xiaowei Zhuang. Three-dimensional super-resolution imaging by stochastic optical reconstruction microscopy. *Science*, 319(5864):810–813, 2008.

[25] Manuel F. Juette, Travis J. Gould, Mark D. Lessard, Michael J. Mlodzianoski, Bhupendra S. Nagpure, Brian T. Bennett, Samuel T. Hess, and Joerg Bewersdorf. Three-dimensional sub-100 nm resolution fluorescence microscopy of thick samples. *Nature Mehtods*, 5(6):527–529, 2008.

[26] H.P. Kao and A.S. Verkman. Tracking of single fluorescent particles in three dimensions: use of cylindrical optics to encode particle position. *Biophysical Journal*, 67(3):1291 – 1300, 1994.

[27] Laurent Holtzer, Tobias Meckel, and Thomas Schmidt. Nanometric three-dimensional tracking of individual quantum dots in cells. *Applied Physics Letters*, 90(5):053902, 2007.

[28] Bo Huang, Sara A. Jones, Boerries Brandenburg, and Xiaowei Zhuang. Whole-cell 3d storm reveals interactions between cellular structures with nanometer-scale resolution. *Nat Meth*, 5(12):1047–1052, 2008.

[29] Sri Rama Prasanna Pavani, Michael A. Thompson, Julie S. Biteen, Samuel J. Lord, Na Liu, Robert J. Twieg, Rafael Piestun, and W. E. Moerner. Three-dimensional, single-molecule fluorescence imaging beyond the diffraction limit by using a double-helix point spread function. *Proceedings of the National Academy of Sciences*, 106(9):2995–2999, 2009.

[30] Majid Badieirostami, Matthew D. Lew, Michael A. Thompson, and W. E. Moerner. Three-dimensional localization precision of the double-helix point spread function versus astigmatism and biplane. *Applied Physics Letters*, 97(16):161103, 2010.

[31] Gleb Shtengel, James A. Galbraith, Catherine G. Galbraith, Jennifer Lippincott-Schwartz, Jennifer M. Gillette, Suliana Manley, Rachid Sougrat, Clare M. Waterman, Pakorn Kanchanawong, Michael W. Davidson, Richard D. Fetter, and Harald F. Hess. Interferometric fluorescent super-resolution microscopy resolves 3d cellular ultrastructure. *Proceedings of the National Academy of Sciences*, 2009.

[32] Natalie de Souza. Optical imaging in thick samples. *Nature Mehtods*, 6(1):35–35, 2009.

[33] Cella Zanacchi, Z. Lavagnino, M. Perrone, A. Del Bue, L. Furia, M. Faretta, and A. Diaspro. Live-cell 3d super-resolution imaging in thick biological samples. *Nature Methods*, pages 1047–1049, December 2011.

[34] Ann McEvoy, Derek Greenfield, Mark Bates, and Jan Liphardt. Q and a: Single-molecule localization microscopy for biological imaging. *BMC Biology*, 8(1):106, 2010.

[35] Atsushi Matsuda, Lin Shao, Jerome Boulanger, Charles Kervrann, Peter M. Carlton, Peter Kner, David Agard, and John W. Sedat. Condensed mitotic chromosome structure at nanometer resolution using palm and egfp-histones. *PLoS ONE*, 5(9):e12768, 2010.

[36] George Patterson, Michael Davidson, Suliana Manley, and Jennifer Lippincott-Schwartz. Superresolution imaging using single-molecule localization. *Annual Review of Physical Chemistry*, 61(1):345–367, 2010.

[37] Osamu Shimomura, Frank H. Johnson, and Yo Saiga. Extraction, purification and properties of aequorin, a bioluminescent protein from the luminous hydromedusan, aequorea. *Journal of Cellular and Comparative Physiology*, 59(3):223–239, 1962.

[38] Mike Heilemann, Sebastian van de Linde, Mark Schttpelz, Robert Kasper, Britta Seefeldt, Anindita Mukherjee, Philip Tinnefeld, and Markus Sauer. Subdiffraction-resolution fluorescence imaging with conventional fluorescent probes. *Angewandte Chemie International Edition*, 47(33):6172–6176, 2008.

[39] S. W. Hell and M. Kroug. Ground-state-depletion fluorscence microscopy: A concept for breaking the diffraction resolution limit. *Applied Physics B: Lasers and Optics*, 60:495–497, 1995. 10.1007/BF01081333.

[40] Jonas Folling, Mariano Bossi, Hannes Bock, Rebecca Medda, Christian A Wurm, Birka Hein, Stefan Jakobs, Christian Eggeling, and Stefan W Hell. Fluorescence nanoscopy by ground-state depletion and single-molecule return. *Nat Meth*, 5(11):943–945, 2008.

[41] S. van de Linde, Anna Loschberger, Teresa Klein, Meike Heidbreder, M. Heilemann, and M. Sauer. Direct stochastic optical reconstruction microscopy with standard fluorescent probes. *Nature Protocols*, 6(7):991–1009, 2011.

[42] Sebastian van de Linde, Ivan Krstic, Thomas Prisner, Soren Doose, Mike Heilemann, and Markus Sauer. Photoinduced formation of reversible dye radicals and their impact on super-resolution imaging. *Photochem. Photobiol. Sci.*, 10:499–506, 2011.

[43] Mike Heilemann, Emmanuel Margeat, Robert Kasper, Markus Sauer, and Philip Tinnefeld. Carbocyanine dyes as efficient reversible single-molecule optical switch. *Journal of the American Chemical Society*, 127(11):3801–3806, 2005.

[44] Riccardo Nifosi, Aldo Ferrari, Caterina Arcangeli, Valentina Tozzini, Vittorio Pellegrini, and Fabio Beltram. Photoreversible dark state in a tristable green fluorescent protein variant. *The Journal of Physical Chemistry B*, 107(7):1679–1684, 2003.

[45] G. Chirico, F. Cannone, A. Diaspro, S. Bologna, V. Pellegrini, R. Nifosì, and F. Beltram. Multiphoton switching dynamics of single green fluorescent proteins. *Phys. Rev. E*, 70:030901, Sep 2004.

[46] Abuduwayiti Aierken. *Ultra-fast, high-precision image analysis for localization-based super resolution microscopy*. PhD thesis, Helsinki University of Technology.

[47] Karen J. Nordell, Elizabeth M. Boatman, and George C. Lisensky. A safer, easier, faster synthesis for cdse quantum dot nanocrystals. *Journal of Chemical Education*, 82(11):1697, 2005.

[48] Gao Xiaohu, Yuanyuan Cui, Leland Chung, and Shuming Nie. In vivo cancer targeting and imaging with semiconductor quantum dots. *Nature Biotechnology*, 22(8):969–976, 2004.

[49] X. Michalet, F. Pinaud, L. Bentolila, J. Tsay, and J Li. Quantum dots for live cells, in vivo imaging, and diagnostics. *Science*, 307(5709):538–544, 2005.

[50] V Ntziachristos, CH Tung, C Bremer, and R Weissleder. Fluorescence molecular tomography resolves protease activity in vivo. *Nature Medicine*, 8(7):757–761, 2002.

[51] Harinder Arya, Zeenia Kaul, Renu Wadhwa, Kazunari Taira, Takashi Hirano, and Sunil C. Kaul. Quantum dots in bio-imaging: Revolution by the small. *Biochemical and Biophysical Research Communications*, 329(4):1173 – 1177, 2005.

[52] Andrew M Smith, Shivang Dave, Shuming Nie, Lawrence True, and Xiaohu Gao. Multicolor quantum dots for molecular diagnostics of cancer. *Expert Review of Molecular Diagnostics*, 6:231–244, 2006.

[53] Margarida M. Barroso. Quantum dots in cell biology. *Journal of Histochemistry and Cytochemistry*, 59(3):237–251, 2011.

[54] Ute Resch-Genger, Markus Grabolle, Sara Cavaliere-Jaricot, Roland Nitschke, and Thomas Nann. Quantum dots versus organic dyes as fluorescent labels. *Nat Meth*, 5(9):763–775, 2008. 10.1038/nmeth.1248.

[55] Keith Lidke, Bernd Rieger, Thomas Jovin, and Rainer Heintzmann. Superresolution by localization of quantum dots using blinking statistics. *Opt. Express*, 13(18):7052–7062, Sep 2005.

[56] Thomas Dertinger, Mike Heilemann, Robert Vogel, Markus Sauer, and Shimon Weiss. Superresolution optical fluctuation imaging with organic dyes. *Angewandte Chemie International Edition*, 49(49):9441–9443, 2010.

[57] Patrick Hoyer, Thorsten Staudt, Johann Engelhardt, and Stefan W. Hell. Quantum dot blueing and blinking enables fluorescence nanoscopy. *Nano Letters*, 11(1):245–250, 2010.

[58] Wilfried G. J. H. M. van Sark, Patrick L. T. M. Frederix, Dave J. Van den Heuvel, Hans C. Gerritsen, Ageeth A. Bol, Joost N. J. van Lingen, Celso de Mello Doneg, and Andries Meijerink. Photooxidation and photobleaching of single cdse/zns quantum dots probed by room-temperature time-resolved spectroscopy. *The Journal of Physical Chemistry B*, 105(35):8281–8284, 2001.

[59] Claire Max. Adaptive optics and its applications.

[60] Junzhong Liang, Bernhard Grimm, Stefan Goelz, and Josef F. Bille. Objective measurement of wave aberrations of the human eye with the use of a hartmann-shack wave-front sensor. *J. Opt. Soc. Am. A*, 11(7):1949–1957, Jul 1994.

[61] Eugene Hecht. *Optics / Eugene Hecht, with contributions by Alfred Zajac*. Addison-Wesley Pub. Co, Reading, Mass. :, 1987. 2nd ed. Includes indexes. Reprinted with corrections May, 1990. Bibliography: p. 661-664.

[62] Robert J. Noll. Zernike polynomials and atmospheric turbulence. *J. Opt. Soc. Am.*, 66(3):207–211, 1976.

[63] Lisa A. Poyneer, Donald T. Gavel, and James M. Brase. Fast wave-front reconstruction in large adaptive optics systems with use of the fourier transform. *J. Opt. Soc. Am. A*, 19(10):2100–2111, Oct 2002.

[64] R. W. Gerchberg and Owen Saxton. A practical algorithm for the determination of the phase from image and diffraction plane pictures. *Optik*, 35:237–246, 1972.

[65] Bridget M. Hanser, Mats G. L. Gustafsson, David A. Agard, and John W. Sedat. Phase retrieval for high-numerical-aperture optical systems. *Opt. Lett.*, 28(10):801–803, May 2003.

[66] Ross W. Deming. Phase retrieval from intensity-only data by relative entropy minimization. *J. Opt. Soc. Am. A*, 24(11):3666–3679, 2007.

[67] R Henriques, M Lelek, EF Fornasiero, F Valtorta, C Zimmer, and MM. Mhlanga. Quickpalm: 3d real-time photoactivation nanoscopy image processing in imagej. *Nature Methods*, 7(5):2, 2010.

[68] S. Wolter, M. SchTtpelz, M. Tscherepanow, S. Van De Linde, M. Heilemann, and M. Sauer. Real-time computation of subdiffraction-resolution fluorescence images. *Journal of Microscopy*, 237(1):12–22, 2010.

[69] A. Neubeck and L. Van Gool. Efficient non-maximum suppression. In *Pattern Recognition, 2006. ICPR 2006. 18th International Conference on*, volume 3, pages 850–855.

[70] David Baddeley, David Crossman, Sabrina Rossberger, Juliette E. Cheyne, Johanna M. Montgomery, Isuru D. Jayasinghe, Christoph Cremer, Mark B. Cannell, and Christian Soeller. 4d super-resolution microscopy with conventional fluorophores and single wavelength excitation in optically thick cells and tissues. *PLoS ONE*, 6(5):e20645, 2011.

[71] Mike Heilemann, Sebastian vandeLinde, Anindita Mukherjee, and Markus Sauer. Super-resolution imaging with small organic fluorophores. *Angewandte Chemie International Edition*, 48(37):6903–6908, 2009.